

Modern Aspects of Electrochemistry 62

Shriram Santhanagopalan *Editor*

Computer Aided Engineering of Batteries

 Springer

Modern Aspects of Electrochemistry

Volume 62

Series Editors

Constantinos G. Vayenas, Department of Chemical Engineering, University of Patras, Patras, Greece

Ralph E. White, Department of Chemical Engineering, University of South Carolina, Columbia, SC, USA

This well-respected series commenced publication in the early 1950s. Over the years it has earned an excellent reputation by offering high quality reviews of current research into all areas of electrochemistry and electrochemical engineering and their applications. The international magazine *Chemistry & Industry* notes that this series “deserves a place in electrochemistry libraries and should prove useful to electrochemists and related workers.” Starting with Number 43 in the series, two features have been introduced:

- Each volume is thematic and focuses on a new development in the field or reviews a well-established area that is regaining interest.
- Each volume is guest-edited. As in the past, all chapters are topical reviews.

Subjects covered in recent volumes include:

1. Modeling and Numerical Simulations
2. Progress in Corrosion Science and Engineering
3. Electrodeposition: Theory and Practice
4. Electrocatalysis: Theory and Experiments
5. Interfacial Phenomena in Fuel Cell Electrocatalysis
6. Diagnostics and Modeling of Polymer Electrolyte Fuel Cells
7. Applications of Electrochemistry and Nanotechnology in Biology and Medicine

Shriram Santhanagopalan
Editor

Computer Aided Engineering of Batteries

 Springer

Editor

Shriram Santhanagopalan 
National Renewable Energy Laboratory
Golden, CO, USA

This work was supported by the U.S. Department of Energy's Vehicle Technologies Office

ISSN 0076-9924

ISSN 2197-7941 (electronic)

Modern Aspects of Electrochemistry

ISBN 978-3-031-17606-7

ISBN 978-3-031-17607-4 (eBook)

<https://doi.org/10.1007/978-3-031-17607-4>

This is a U.S. government work and not under copyright protection in the U.S.; foreign copyright protection may apply 2023

All rights are solely and exclusively licensed by the Publisher, whether the whole or part of the material is concerned, specifically the rights of translation, reprinting, reuse of illustrations, recitation, broadcasting, reproduction on microfilms or in any other physical way, and transmission or information storage and retrieval, electronic adaptation, computer software, or by similar or dissimilar methodology now known or hereafter developed.

The use of general descriptive names, registered names, trademarks, service marks, etc. in this publication does not imply, even in the absence of a specific statement, that such names are exempt from the relevant protective laws and regulations and therefore free for general use.

The publisher, the authors, and the editors are safe to assume that the advice and information in this book are believed to be true and accurate at the date of publication. Neither the publisher nor the authors or the editors give a warranty, expressed or implied, with respect to the material contained herein or for any errors or omissions that may have been made. The publisher remains neutral with regard to jurisdictional claims in published maps and institutional affiliations.

This Springer imprint is published by the registered company Springer Nature Switzerland AG
The registered company address is: Gewerbestrasse 11, 6330 Cham, Switzerland

Foreword

Mathematical modeling has become a critical component of battery development. New batteries are being developed for a host of applications from consumer electronics to electric vehicles. Consequently, the role of mathematical modeling in designing and building these new battery cells, modules, and packs has become critical. Physics-based battery models are being used extensively to determine design factors that limit the performance of a cell, factors that govern degradation of a given battery design under prescribed operating conditions, and to estimate the remaining useful life of cells and packs. As larger form factors emerge, these models will have to be retooled to incorporate local variations in temperature, resistance build-up, and other heterogeneities. The need for rapid prototyping and scale-up in record turn-around times demanded by the electrification of vehicles has prompted development of a new generation of software tools. These virtual design platforms integrate geometry, performance, life predictions, and safety assessment into a comprehensive suite of mathematical modeling tools that Industry can readily adopt to simulate different case studies to match form factors and chemistries to target applications.

With feedback from various participants in the supply chain, the U.S. Department of Energy initiated a dedicated effort to deploy advanced simulation tools for Computer Aided Engineering for Electric-Drive Vehicle Batteries (CAEBAT). The program was built upon years of phenomenological model development efforts by world-class teams comprised of technical experts on mathematical model development, software companies, and end users with active collaboration from Industry, Academia, and several National Laboratories. Since then, these tools have been extensively licensed around the world. This volume is a compilation of some highlights from this effort.

This volume highlights the rampant growth of the battery modeling industry giving practical examples of the different toolsets available in the market and how these have been utilized progressively by the scientific community. There are instances of current-density distribution measurements that have dominated the literature on classic electrochemical engineering for decades, and how these are relevant to evaluate design features in commercial cells of different formats using

detailed multidimensional performance models. With access to higher resolution measurements, quantifying the effects of local heterogeneity at the electrode level is no longer deemed a mathematical curiosity. Advances in both experiments and mathematical models are discussed with detailed examples. There are several instances of deploying mathematical battery models for commercial use covered by experts in Industry. Starting out with the Multi-Scale Multi-Domain models that decouple the geometric design of the cell from chemistry-related parameters, this volume shows practical examples of commercial cell and module design, providing extensive validation across length scales. Calibration of model parameters, especially for difficult to obtain mechanical and thermal abuse cases, is discussed at length. The complex interplay of mechanical, thermal, and electrochemical phenomena in determining a given cell or module design is highlighted with practical examples. Gaps in understanding battery safety are also called out using detailed phenomenological models. This volume concludes with an emphasis on the high-performance computing aspects of battery modeling, which is an emerging trend. This chapter provides tangible examples of scale-bridging and discusses opportunities for data science and machine learning in this data-rich discipline.

Overall, mathematical battery modeling has come a long way in terms of the sophistication in how the technical details are represented, ease of adoption, as well as widespread use. As newer cell formats, chemistries, and applications emerge, this field has grown exponentially to help navigate gaps in our understanding of the material limitations for example. With increased emphasis on virtual development and monitoring platforms, the mathematical battery modeling community has evolved drastically to enable deployment of real-time fault-monitoring systems. Reliability improvements assisted by extensive mathematical modeling and analysis of large datasets using an automated pipeline of software tools are becoming the norm. This volume provides a comprehensive overview of the state-of-the-art in mathematical battery modeling with an emphasis on practically relevant solutions.

Columbia SC, USA

Ralph E. White

Preface

Building a battery has remained as much an art, as it has been precise engineering through several generations of cell formats, applications, and chemistries. As with any intricately well-designed system, the scale and range of complexities at the cross-roads of multiple disciplines provides for a rich set of challenges to tackle.

A carefully thought-out program was initiated by the Vehicle Technologies Office at the U.S. Department of Energy, with the intent of employing simulation tools to support technically rigorous and cost-effective design of automotive batteries. Since their inception, the Computer Aided Engineering for Electric-Drive Vehicle Batteries (CAEBAT) umbrella of projects have significantly influenced battery manufacturers, original equipment manufacturers (OEMs), and academic researchers alike. The suite of tools deployed under this effort have been focused on minimizing the build-and-break cycles associated with battery design while shedding light on the nuances of process engineering and how they relate to battery performance in the long run. This volume attempts to provide an up-close look at several aspects of modeling the performance, life, and safety response of batteries. Building upon a strong foundation of physics-based models, the emphasis is on delivering practical tools for the broader battery community.

We did not attempt to cover every aspect of the different projects under CAEBAT, but rather provide a flavor of how virtual design tools for large format batteries have evolved under the program. References to earlier publications and webpages are provided throughout the volume for readers to get a comprehensive understanding of the models. Chapter 1 provides an excellent overview of the broad range of computational tools and commercial software that cater to battery engineering. Beyond discussing the capabilities of the various software tools, this chapter also serves as an authoritative compilation of the battery modeling literature. Detailed experimental investigations of heterogeneities in large format cells are discussed in Chap. 2. These one-of-a-kind measurements help us understand thermal and electrical limitations across different parts of the cell. The corresponding models address practical questions that are relevant to scaling up of cell formats. Chapter 3 provides a thorough discussion of electrode engineering that highlight the importance of design at the mesoscale across multiple battery chemistries. These

timeless examples showcase the utility of these models for next-generation battery chemistries. Chapter 4 carefully considers aspects of pack design providing a lot of experimental results that call attention to the maturity of these modeling tools and relevance to practical automotive battery design. Chapter 5 covers some of the most detailed experimental studies on parameterizing mechanical response of batteries, from cell components all the way to modules. This chapter calls for attention to detail when setting up abuse tests and provides specific recommendations on minimizing variability in the test results. In Chap. 6 we discuss our experiences simulating mechanical deformation under a variety of abuse conditions. We address some issues frequently called out in this discipline, such as the relationship between contact resistances and heat generation rates or the influence of aging on the abuse response of the cells. Chapter 7 emphasizes multi-scale models and high-performance computing tools to streamline their implementation. The chapter closes out with a detailed discussion of how artificial intelligence and machine learning tools interface with large databanks to redefine computer aided battery engineering. Together, these chapters provide a well-rounded approach to computational design of batteries.

Lastly, this is very much an effort in progress. Alongside newer chemistries, mathematical tools to facilitate battery design and analysis are growing by leaps and bounds. We earnestly hope that the chapters help as much in raising the bar as they do set the stage up for robust design of batteries.

Golden, CO, USA

Shriram Santhanagopalan

Acknowledgments

We acknowledge both technical and financial support from the Vehicle Technologies Office at the Department of Energy's Office of Energy Efficiency and Renewable Energy (EERE) for the Computer Aided Engineering for Electric-Drive Vehicle Batteries (CAEBAT) program under Agreement No. 29834. Special thanks are due to our Program Managers David Howell and Brian Cunningham for the visionary conception of the program to develop a state-of-the-art virtual platform for design and analysis of large format batteries. Funding from U.S. Army TARDEC (now GVSC) under Agreement No. MIPR 11037569/2810215 (Yi Ding) is gratefully acknowledged. Constant support and incessant encouragement from NREL Management, especially, John Green, Chris Gearhart, and John Farrell were key enablers in pursuing such a diverse range of projects. Ahmad Pesaran at NREL and John Turner at ORNL were instrumental in assembling, coordinating, and leading the different teams under CAEBAT. Both their years of experience and close work with the relevant partners from Industry were key to the success of the program. Ted Miller from the Ford Motor Company and Mary Fortier from General Motors were early champions of this effort and provided unparalleled access to world-class technical resources. Unwavering support from members of the USABC Technical Advisory Committee, the Crash Safety Work Group, battery companies, and software developers who worked with us providing samples, sharing their technical insights and the needs from the industry deserve our sincere appreciation. We are deeply indebted to our colleagues (current and previous) at NREL for their excellent technical contributions.

Contents

1 Applications of Commercial Software for Lithium-Ion Battery Modeling and Simulation	1
Robert Spotnitz	
2 In Situ Measurement of Current Distribution in Large-Format Li-Ion Cells	31
Guangsheng Zhang, Christian E. Shaffer, Xiao Guang Yang, Christopher D. Rahn, and Chao-Yang Wang	
3 Mesoscale Modeling and Analysis in Electrochemical Energy Systems	69
Venkatesh Kabra, Navneet Goswami, Bairav S. Vishnugopi, and Partha P. Mukherjee	
4 Development of Computer Aided Design Tools for Automotive Batteries	119
Taeyoung Han and Shailendra Kaushik	
5 Experimental Simulations of Field-Induced Mechanical Abuse Conditions	187
Loraine Torres-Castro, Sergiy Kalnaus, Hsin Wang, and Joshua Lamb	
6 Abuse Response of Batteries Subjected to Mechanical Impact	199
Jinyong Kim, Anudeep Mallarapu, and Shriram Santhanagopalan	
7 Accelerating Battery Simulations by Using High Performance Computing and Opportunities with Machine Learning	243
Srikanth Allu, Jean-Luc Fattbert, Hsin Wang, Srdjan Simunovic, Sreekanth Pannala, and John Turner	
Index	273

Chapter 2

In Situ Measurement of Current Distribution in Large-Format Li-Ion Cells



Guangsheng Zhang, Christian E. Shaffer, Xiao Guang Yang, Christopher D. Rahn, and Chao-Yang Wang

Abstract Non-uniform current distributions in large-format Li-ion cells can cause underutilization of active materials, reduction of usable energy density, non-uniform heat generation, exacerbated lithium plating, and accelerated degradation. In situ measurements of current distributions in large-format Li-ion cells not only reveal local behaviors but also provide spatially resolved data for validation of electrochemical-thermal coupled models. The insights and models aid the development of faster rechargeable, energy denser, safer, and more durable Li-ion batteries. This work reviews the progress of in situ measurement of current distribution over the electrode area for large-format Li-ion cells. Direct measurement using segmented cells, indirect measurement using embedded local potential tabs, and noninvasive diagnosis with magnetic resonance imaging are discussed. Key findings from the measurements are then summarized, such as the current distributions under

Statement Parts of this chapter are reproduced with permission from Zhang et al. (2013) *J. Electrochem. Soc.* 160, A610 and Zhang et al. 2013 *J. Electrochem. Soc.* 160, A2299, Copyright 2013 The Electrochemical Society.

G. Zhang (✉)

Department of Mechanical & Aerospace Engineering, The University of Alabama in Huntsville, Huntsville, AL, USA

e-mail: gz0002@uah.edu

C. E. Shaffer · X. G. Yang

Electrified Powertrain Engineering, Ford Motor Company, Dearborn, MI, USA

C. D. Rahn

Battery and Energy Storage Technology Center and Department of Mechanical Engineering, The Pennsylvania State University, University Park, PA, USA

C.-Y. Wang

Electrochemical Engine Center (ECEC) and Department of Mechanical Engineering, The Pennsylvania State University, University Park, PA, USA

This is a U.S. government work and not under copyright protection in the U.S.; foreign copyright protection may apply 2023

S. Santhanagopalan (ed.), *Computer Aided Engineering of Batteries*,

Modern Aspects of Electrochemistry 62,

https://doi.org/10.1007/978-3-031-17607-4_2

various operating conditions and cell designs, and the effects of non-uniform current distributions on local state of charge and usable energy density. Finally, future research needs are proposed.

2.1 Introduction

Since its commercialization in the early 1990s, Li-ion battery technology quickly dominated and advanced the portable electronics industry with advantages of high energy density, low self-discharge, and long cycle life [1–2]. In the past decade, its application in electric vehicles has proliferated to enable a sustainable energy future [3]. As compared to applications in portable electronics, Li-ion batteries in electric vehicles are much larger in size and more demanding in terms of energy density, power density, safety, durability, and cost. Although much progress has been made, grand challenges remain [4–5]. In particular, how to unlock the potential of Li battery materials and to scale up Li-ion cells to hundreds of Ah per cell without substantial losses in power performance, durability, and safety remains a key technological challenge. This challenge is exacerbated by the increasing demand of fast charging [6–9], low temperature operation [10], high energy density, and robust safety [11–13] driven by wider adoption of electric vehicles in recent years.

As schematically shown in Fig. 2.1, in large-format Li-ion cells, especially cylindrical and prismatic ones with long current collectors and limited tabs [14–15], the path of current through thin metal foil current collectors is not equal at different locations along the electrodes. Through complex interactions among the local reaction current, state of charge (SOC), and temperature, non-uniform spatial distribution of these parameters is inevitable, especially during high rate charging and discharging. Such non-uniform distributions will lead to underutilization of active materials loaded in a large cell, thereby drastically reducing its energy density from the coin cell benchmark [15]. Of equal importance, non-uniform current distribution can exacerbate localized lithium plating during fast charging and localized overheating during high rate operation, compromising durability and safety of large batteries. Therefore, understanding how these critical parameters

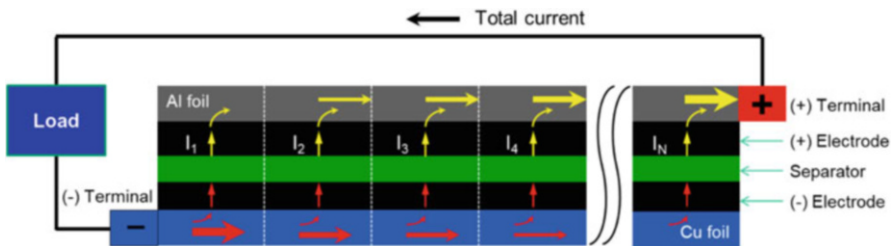


Fig. 2.1 Schematic of current flow path in a Li-ion cell with a pair of counter located terminals during discharging (the schematic is not to scale)

distribute under various design and operation conditions greatly aids development of faster rechargeable, energy denser, safer, and more durable Li-ion batteries.

Modeling has been widely used in the research and development of Li-ion cells to gain insight into electrochemical-thermal coupled phenomena, predict cell performance and aging, optimize cell design and operation, and accelerate development of new concepts and strategies [15–26]. But these models need to be validated against experimental data to be reliable. Considering that critical internal parameters of local current density, SOC, and temperature are non-uniformly distributed spatially and temporally in large-format Li-ion cells, multidimensional models need to be validated against not only overall performance data but also spatially distributed data.

Therefore, it is important to experimentally measure current density, SOC, and temperature in large-format Li-ion cells locally, in order to reveal insight about their distribution characteristics and to provide spatially resolved data for multi-dimensional model validation. Considering that distribution of those parameters is transient in nature, in situ measurement is desired.

Supported by US Department of Energy's CAEBAT program, a research team at EC Power and The Pennsylvania State University (PSU) measured current distributions in situ along electrode length using a segmented cell approach [27–28]. Based on the measured current distributions, SOC distributions were obtained. The team also in situ measured temperature distributions in Li-ion cells [29–30]. The measurement revealed many insights on Li-ion cells and provided spatially resolved data for model validation [15]. Since then other work on current distribution measurement have been reported using Li-ion cells with embedded local potential measurement tabs [31–33] or using noninvasive magnetic resonance imaging (MRI) for commercial Li-ion cells [34]. However, further efforts are still needed on this important topic. In particular, behaviors of current distribution under extreme conditions with emerging battery materials or designs are not well understood in spite of their importance to wide adoption of electric vehicles, such as extreme fast charging [9], low temperature operation [10], and safety abuse conditions [35].

Note that non-uniformity of current distribution in Li-ion batteries exists at various levels, including module level consisting of parallel-connected cells [36–37], cell level along electrode length [27–28, 33–34, 38], and electrode level across electrode thickness [39–41]. In this work, we focus on in situ measurement of current distribution at cell level along electrode length which is special to large-format Li-ion cells. In Sect. 2.2, we review the work of direct measurement using segmented Li-ion cells by the EC Power-PSU team. In Sect. 2.3, we review the work of indirect measurement using embedded local potential tabs [31–33]. In Sect. 2.4, we review the work of noninvasive diagnosis with magnetic resonance imaging [34]. In Sect. 2.5, we briefly summarize the progress and propose further efforts to address the emerging needs of electric vehicle Li-ion cells.

2.2 Direct Measurement of Current Distribution Using Segmented Li-Ion Cells

As indicated in Fig. 2.1, if one or both electrodes in a Li-ion cell are electrically segmented, for example, along the dashed lines, local currents in each segment would be forced to flow separately, allowing direct measurement of current distribution. The EC Power-PSU team took this approach. This section is a summary of the work by the team, including both published [27–28] results and previously unpublished results (Sects. 2.2.2.6, 2.2.2.7 and 2.2.2.8).

2.2.1 Experimental Method Using Segmented Li-Ion Cells

2.2.1.1 Experimental Cell with Segmented Positive Electrode

Figure 2.2 shows schematically the experimental cell used in studies by the EC Power-PSU team [27–28]. The experimental cell consists of one intact negative electrode (with active material coated on both sides of a Cu foil), two layers of separators, and ten positive electrode segments (with active material coated on both sides of an Al foil). The negative electrode has only one tab, which serves as the negative terminal of the cell. Every positive electrode segment has two tabs, with only one tab per segment used in study [27] and both tabs per segment used in study [28]. The intact negative electrode and separators are folded in a serpentine manner, (Z-fold) with one positive electrode segment sandwiched inside each fold.

In the experimental cell, positive and negative electrode active materials are lithium iron phosphate (LFP) and graphite, respectively. The separator is Celgard[®] 2320 PP/PE/PP membrane (20 μm thick). The electrolyte is 1.2 M LiPF_6 in EC:EMC:PC (45:50:5 v%). The positive electrode coating (each side) is 64 μm thick, and negative electrode is 43 μm thick. The Al foil current collector is 15 μm thick, and the Cu foil is 10 μm thick. Every positive electrode segment is 150 mm long and 56.5 mm wide (the coated area). The negative electrode is ~ 1.8 m long. The electrode-separator sandwich is assembled in a pouch. After electrolyte filling, the pouch cell is sealed with 1 negative terminal and 20 positive terminals exposed to the outside. The cell has a nominal capacity of 2.4 Ah.

2.2.1.2 Experimental System

Figure 2.3 shows a schematic of the experimental system in study [27]. Note that the experimental Li-ion cell is shown unfolded and simplified in the schematic for clarity. The ten positive electrode segments are connected in parallel to a low-resistance bus wire, each through a shunt resistor (PLV7AL, 2 $\text{m}\Omega \pm 0.5\%$, Precision Resistor Co., USA) for local current sensing. A low resistance meter (3560, Hioki, Japan) is used to ensure that the resistance of shunt and connecting

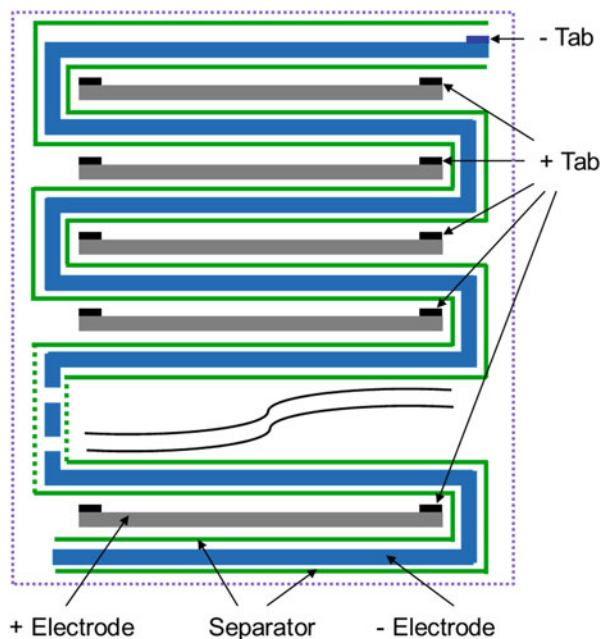


Fig. 2.2 Schematic of experimental Li-ion cell with segmented positive electrode (not to scale). (Adapted with permission from Ref. [27] Copyright 2013 The Electrochemical Society)

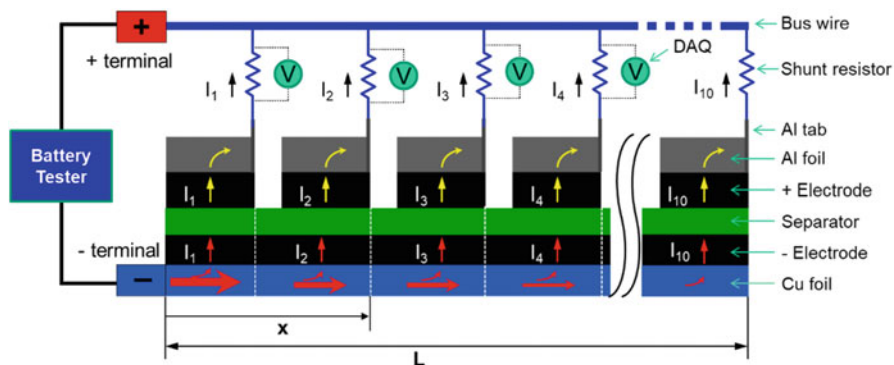


Fig. 2.3 Schematic of experimental system for current distribution measurement (The experimental Li-ion cell is shown unfolded and simplified in the schematic for clarity; arrows represent current flow during discharge). (Reused with permission from Ref. [27] Copyright 2013 The Electrochemical Society)

wires is the same for every channel ($4.0 \pm 0.1 \text{ m}\Omega$) and resistance of the bus wire is negligible ($<0.1 \text{ m}\Omega$). By connecting the positive electrode segments in parallel and making resistance from the positive terminal bus to the Al tab uniform for each local channel, the effects of Al foil on current distribution can be suppressed so

as to focus on the effects of the Cu foil current collector. Note that DC internal resistance of each cathode segment and corresponding anode is estimated to be more than 800 m Ω using a method based on cell open circuit voltage and cell voltage at 10 s into C/5 discharge at room temperature [42]. Therefore, the influence of additional resistance from the shunt resistor (4.0 ± 0.1 m Ω) is negligibly small as compared with the DC internal resistance of each segment. Also note that in present-day designs, commercial Li-ion cells with negative electrodes as long as 1.8 m would rarely have only one tab for the electrode due to excessive resistance. So the current distribution in this experimental Li-ion cell is more non-uniform than that in a commercial cell with similar size. But the mechanisms of non-uniform current distribution due to current collector resistance are the same. The experimental setup in this study can separate and amplify the effects of the current collector to reveal insights on current distribution in Li-ion cells. Even for commercial Li-ion cells, the resistance of current collectors can influence current distribution during high current charging and discharging. The experimental setup in study [28] has different tab configurations, which will be described in Fig. 2.17.

2.2.2 Results from Segmented Li-Ion Cell

2.2.2.1 Overall Cell Performance

Figure 2.4 shows voltage of the experimental cell during discharge at various C rates [27]. Open circuit voltage (OCV) of the cell at different stages of discharge is also shown, which are obtained by discharging the cell at C/10 intermittently followed

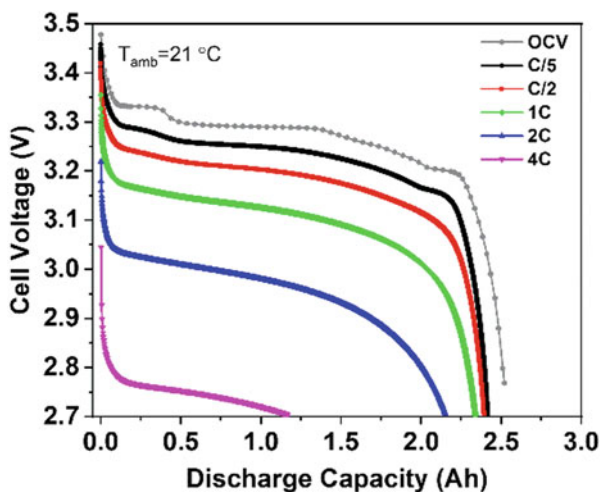


Fig. 2.4 Voltage of the experimental Li-ion cell during discharge at various C rates at room temperature (21 °C). (Adapted with permission from Ref. [27] Copyright 2013 The Electrochemical Society)

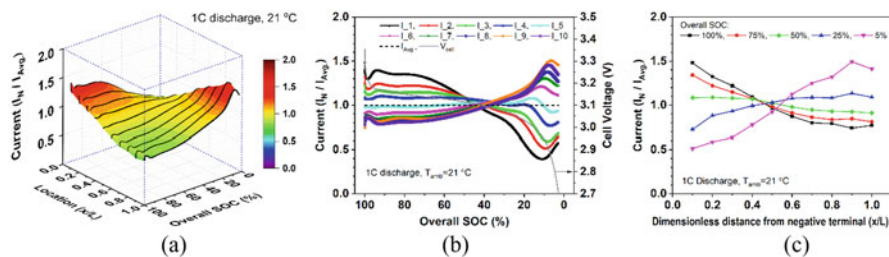


Fig. 2.5 Spatial-temporal current distribution during 1C discharge at 21 °C. (a) Variation of local currents with both location and overall SOC; (b) Variation of local currents and cell voltage with overall SOC; (c) Spatial current distribution at different SOC. (Adapted with permission from Ref. [27] Copyright 2013 The Electrochemical Society)

by a rest period of 1 h. The cell voltage and discharge capacity decreased with increasing C rate, which was attributed to higher ohmic and kinetic overvoltage at higher current. The OCV variation was attributed primarily to open circuit potential (OCP vs. Li/Li^+) variation of graphite [43] because LFP has a flat OCP curve in a wide range of state of charge (SOC) [44].

2.2.2.2 Current Distribution During 1 C Discharge at Room Temperature

Figure 2.5a shows the measured spatial-temporal current distribution during 1C discharge at room temperature (21 °C). Note that local currents are made dimensionless after being normalized by the average current for convenient comparison among different cases. The discharge time is made dimensionless by using the cell overall SOC to indicate discharge progress. Location of each segment is made dimensionless using relative distance from the negative terminal of the experimental Li-ion cell. Figure 2.5b shows temporal variation of each local current, with average current (equal to the unity after normalization) and cell voltage also shown in the figure. Figure 2.5c shows spatial distribution of local currents at different levels of cell SOC, using the local currents data extracted from Fig. 2.5b. Current distribution is not uniform from beginning of discharge and evolves significantly as discharge proceeds. Initially, segments closer to the negative terminal produce higher local currents than those farther away, i.e., $I_1 > I_2 > I_3 \dots > I_{10}$. As discharge continues, local currents in segments with higher initial values generally decrease, while those with lower initial values increase, which leads to an entirely different pattern of current distribution near the end of discharge ($I_1 < I_2 < I_3 \dots$). Note that I_9 is almost always slightly higher than I_{10} , which was attributed to that segment 9 had slightly higher capacity than other segments [27].

The very non-uniform current distribution at the beginning of discharge was attributed to the resistance of the negative current collector ($\sim 55 \text{ m}\Omega$) [27]. As schematically shown in Fig. 2.3, current flows in the Cu foil from the negative terminal to the other end and gradually decreases along the flow direction as

local currents enter the negative electrode. As the current flows in, considerable potential drop along the Cu foil occurs due to its resistance. On the other hand, potentials of segments on the positive side (joint of shunt resistor with bus wire) are essentially equal due to negligible resistance of the bus wire. Consequently, the local overvoltage is smaller for segments farther from the negative terminal, thereby driving lower current according to electrochemical kinetics (e.g., Butler-Volmer equation) [45]. Therefore, the farther a segment is from the negative terminal, the smaller the local overvoltage is, and the lower current it generates. Higher SOC remains in regions far away from the negative terminal.

As discharge proceeds, the regions farther away from the negative terminal maintain higher SOC, and thus higher OCV, due to less current generation earlier and hence produce higher local currents later. The dramatic variation of local currents during late stages of discharge can be attributed to the counteracting effects between potential drop along the Cu foil and the local SOC (or OCV) non-uniformity. The two effects counteract, tending to balance the current distribution. Therefore, local currents in segments with higher initial values would decrease, while local currents in segments with lower initial values would increase. When the effect of local SOC (or OCV) overrides the effect of the ohmic potential drop along the Cu foil, in the case near the end of discharge, the current distribution would reverse in pattern, becoming entirely different from that at the beginning of discharge. As will be shown in Fig. 2.11a, local SOC during discharge can be estimated from local currents data, and the results agree with this explanation very well.

2.2.2.3 Effects of Discharging C Rate on Current Distribution

Discharge C rate was found to have significant effects on current distribution [27]. Figures 2.6 and 2.7 show results of current distribution during C/5 and 4C

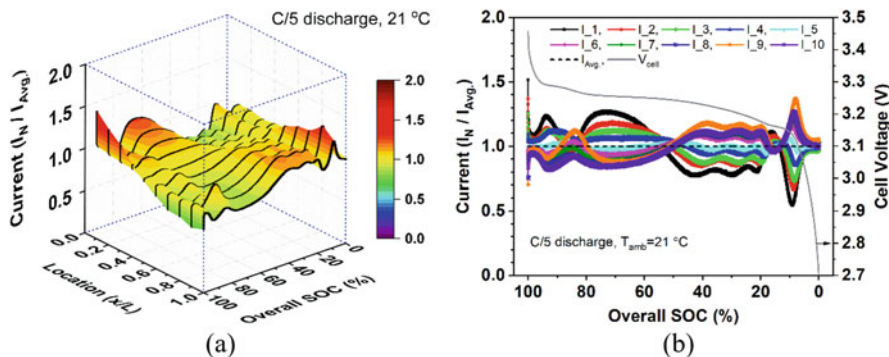


Fig. 2.6 Current distribution during C/5 discharge at 21 °C. (a) Variation of local currents with both location and overall SOC; (b) Variation of local currents and cell voltage with overall SOC. (Adapted with permission from Ref. [27] Copyright 2013 The Electrochemical Society)

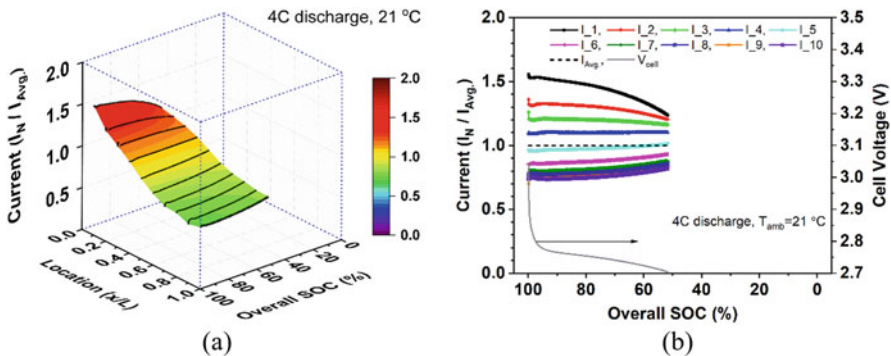


Fig. 2.7 Current distribution during 4C discharge at 21 °C. (a) Variation of local currents with both location and overall SOC; (b) Variation of local currents and cell voltage with overall SOC. (Adapted with permission from Ref. [27] Copyright 2013 The Electrochemical Society)

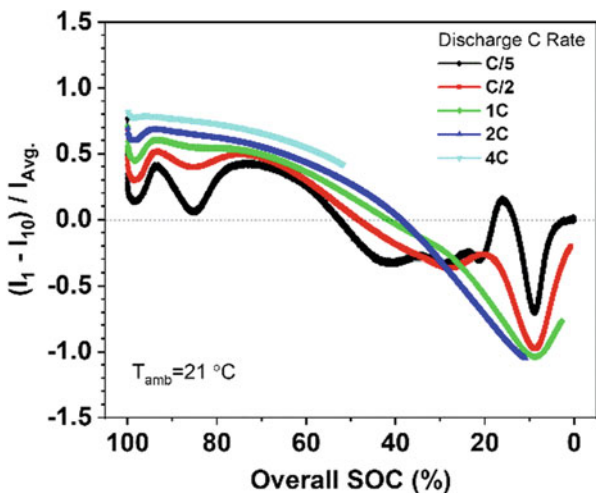


Fig. 2.8 Maximum difference in local current during different C rate discharge at 21 °C. (Adapted with permission from Ref. [27] Copyright 2013 The Electrochemical Society)

discharge, respectively, for comparison with results at 1C. It can be seen clearly that local currents spread less during lower C-rate discharge, indicating more uniform current distribution. This trend can be more clearly seen from Fig. 2.8, in which the differences between I_1 and I_{10} during different C rate discharge are plotted together. Segments 1 and 10 are most apart along the negative current collector, and I_1 and I_{10} are most different, so their difference, i.e., the maximum ΔI , can be used to represent the non-uniformity of current distribution in the experimental cell.

The effects of C-rate on current distribution were also attributed to the opposing effects of potential drop along the Cu foil and the local SOC (or OCV) non-uniformity [27]. During low C rate discharge (C/5), potential drop along the Cu

foil is so small that the local current distribution is controlled by local SOC (or OCV) non-uniformity. Indeed, a wavy pattern, evident from Figs. 2.6 and 2.8 results, reflective of multiple plateaus and frequent slope changes seen in the OCV vs. SOC curve. During high C rate discharge (4C), the potential drop along the Cu foil, amounting to ~20 times larger than that during C/5 discharge, would dominate the local current distribution. This dominance by the ohmic potential drop creates smoothly varying patterns, as can be seen clearly from Fig. 2.8 for the cases of 1C, 2C, and 4C. It was hypothesized that a battery operated in close vicinity to the equilibrium features a wavy current distribution, while a battery operated far away from the equilibrium would exhibit a monotonic variation.

2.2.2.4 Effects of Ambient Temperature

Ambient temperature was also found to have significant influences on current distributions [27]. Figures 2.9 and 2.10 show the current distribution at 0 °C and 45 °C during 1C discharge. Comparison with the results at 21 °C, as shown in Fig. 2.5, clearly indicates lower overall performance but more uniform current distribution at lower ambient temperature. This interesting phenomenon can be mainly attributed to the effects of temperature on the internal resistance of Li-ion battery cells, which includes the ohmic resistance, the charge transfer resistance, the resistance of SEI, and mass transport resistances. Previous studies show that the charge transfer resistance, SEI resistance [46–47], and electrolyte resistance [48] increase dramatically at lower temperature while the ohmic resistance of the Al and Cu foils change little (actually decrease slightly [49]). Using open circuit voltage and cell voltage at 10 s of discharge, it can be estimated that internal resistance of the cell at 0 °C is approximately 60% higher than that at 21 °C. As suggested in Fig. 2.3, higher battery sandwich resistance at lower temperature would make the effects of ohmic potential drop along the Cu and Al foils less significant on the

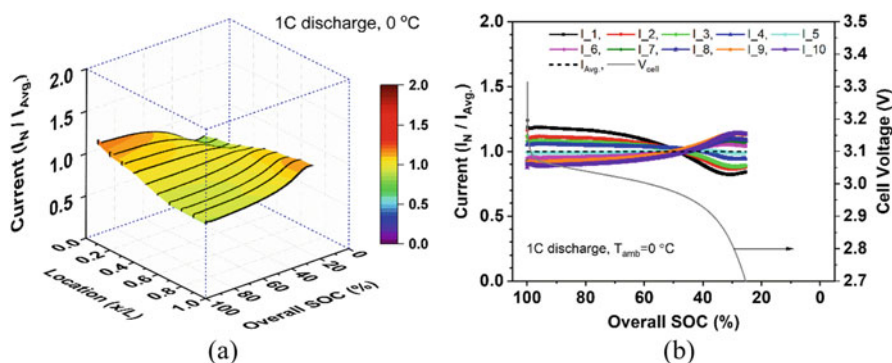


Fig. 2.9 Current distribution during 1C discharge at 0 °C. (a) Variation of local currents with both location and overall SOC; (b) Variation of local currents and cell voltage with overall SOC. (Adapted with permission from Ref. [27] Copyright 2013 The Electrochemical Society)

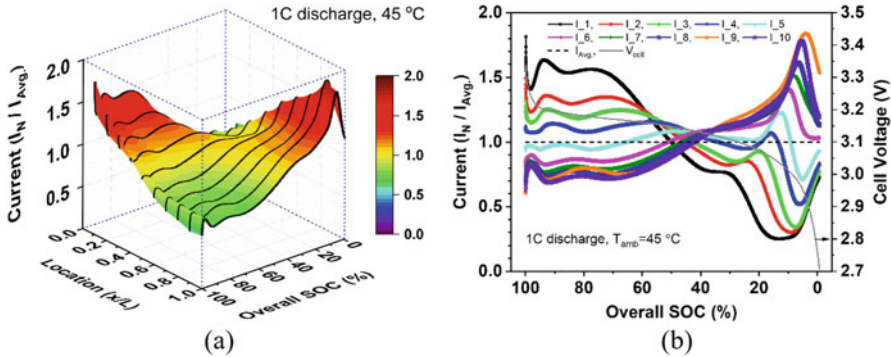


Fig. 2.10 Current distribution during 1C discharge at 45 °C. (a) Variation of local currents with both location and overall SOC; (b) Variation of local currents and cell voltage with overall SOC. (Adapted with permission from Ref. [27] Copyright 2013 The Electrochemical Society)

current distribution. Therefore, the current distribution would be more uniform at lower temperature. Obviously, higher internal resistance would reduce the overall performance of the experimental cell due to higher overvoltage at the same current. The cell resistance at 45 °C is estimated to be approximately 25% lower than that at 21 °C, so the better overall performance yet more non-uniform current distribution at 45 °C also agrees with the explanations.

2.2.2.5 Local SOC Distribution Calculated from Current Distribution Data

With information on local currents, discharged capacity of every segment was calculated by integrating local current in time from beginning of discharge. Then local SOC was obtained by taking capacity of local segment during C/5 discharge as reference of SOC = 100% [27]. Figure 2.11a shows distribution of local SOC at different overall SOC during 1C discharge. As expected, the SOC distribution first becomes more and more non-uniform as discharge proceeds due to the higher local currents closer to the negative terminal, and then the SOC distribution becomes less non-uniform as discharge approaches end of discharge due to the reversal of current distribution.

It is interesting to note that the SOC distribution is still not uniform at cutoff for 1C discharge. This phenomenon is even more obvious at higher C rates, as can be seen from Fig. 2.11b, which shows SOC distribution at cutoff for different C rate discharge. For the 4C discharge, local SOC of segment 1 is around 30%, while that of segment 10 is higher than 60%. Such highly non-uniform SOC distribution at cutoff significantly underutilizes the active materials loaded in the battery, thereby reducing its energy density. Indeed, the very high SOC of segment 10 suggests that active materials in certain locations are largely underutilized, a significant waste of battery materials.

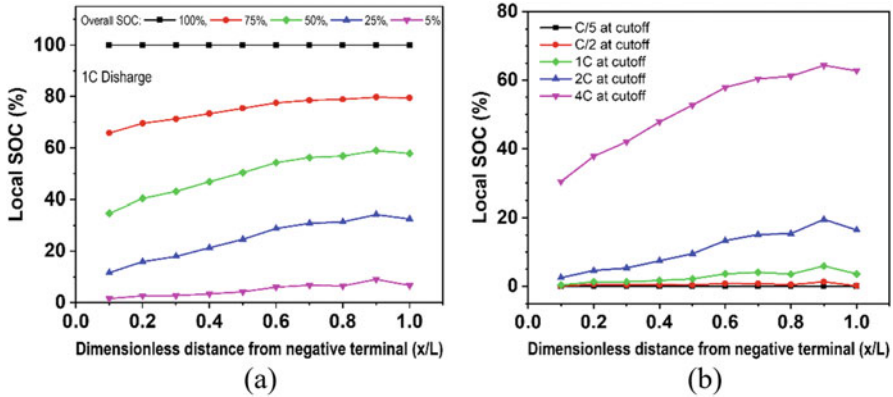


Fig. 2.11 (a) Local SOC distribution at different overall SOC during 1C discharge at 21 °C; (b) Local SOC distribution at cutoff during different C rate discharge at 21 °C. (Adapted with permission from Ref. [27] Copyright 2013 The Electrochemical Society)

2.2.2.6 Internal Balancing Current After Discharge and Its Effects on Local SOC Distribution

Li-ion cell OCV depends on SOC. Figure 2.12 shows such dependence for the experimental Li-ion cell. It is clear that the OCV generally decreases with SOC except a few plateaus as typical for LFP-Graphite cell. The non-uniform local SOC distribution at cutoff shown in Fig. 2.11 suggests non-uniform local OCV. As schematically shown in Fig. 2.12, such local OCV difference would cause internal balancing current flow. For example, the local SOC of segment 1 is around 30%, while that of segment 10 is higher than 60% at the end of 4C discharge. The local OCV of segment 1 would be nearly 40 mV lower than that of segment 10. Such an OCV difference would drive internal current flow between segment 1 and segment 10 until their OCV become the same. During the balancing process, segment 1 would be charged, while segment 10 is being discharged. Similar phenomena would occur to other segments depending on the OCV difference.

The internal balancing currents were indeed observed in the experiments. Figure 2.13a, b shows the internal balancing current after 1C discharge and 4C discharge, respectively. To reflect the magnitude of internal balancing current, local C rate is used. Note that during balancing, the total current is zero, while local currents are negative or positive. Positive local current means the corresponding segment is being discharged, while a negative local current means the segment is being charged. It can be seen that in both cases, segments closer to negative terminal (1–4) are charged, while segments further away from the negative terminal (6–10) are discharged, corresponding to the non-uniform SOC distribution shown in Fig. 2.11. It is interesting to note that internal balancing takes longer time after higher C rate discharge. After 1C discharge, it took less than 1200 s for all local internal balancing currents to become smaller than 1 mA ($C/240$). In comparison, after 4C discharge,

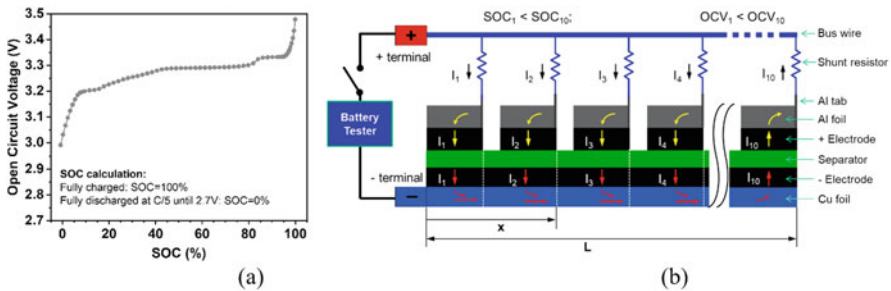


Fig. 2.12 (a) OCV of the experimental Li-ion cell at different SOC; (b) Schematic of internal balancing current flow in experimental Li-ion cell after discharge

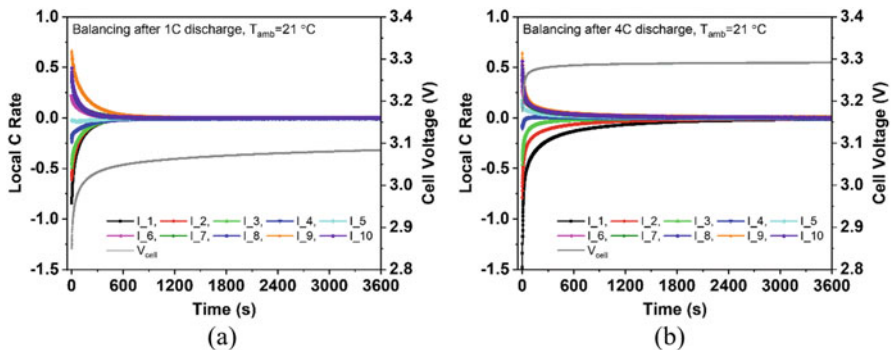


Fig. 2.13 Local internal balancing currents and cell voltage (a) after 1C discharge and (b) after 4C discharge

the internal balancing current in segment 1 was still larger than 1 mA after 3600 s of rest. It is also interesting to note that the recovery of OCV corresponds to decrease of internal balancing current, suggesting that internal balancing current plays an important role in OCV recovery during rest.

As expected, the internal balancing currents reduce non-uniformity of local SOC distribution. Figure 2.14 shows the cell local SOC_s at cutoff voltage (solid lines) and after balancing (dashed lines, after all local currents become smaller than 1 mA). Notably, in Fig. 2.14, the 1C green curves correspond with the resting highlighted in Fig. 2.13a, and the 4C magenta curves correspond with the resting shown in Fig. 2.13b. For the 1C discharge, we observe in Fig. 2.14 that the cell SOC is nearly uniform after balancing. However, it is important to note in Fig. 2.13a that after 3600 s of rest, the cell voltage is still recovering toward ~3.1 V at a rate of 5 $\mu\text{V/s}$. The relatively quick balancing of the local SOC after 1C discharge (compared with the 4C discharge) can no doubt be attributed in part to the fact that the cell was not significantly out of balance at the end of the 1C discharge. However, the observation that the voltage is still recovering as the cell nears a state of balance is an interesting one. This can most likely be attributed to the significant slope

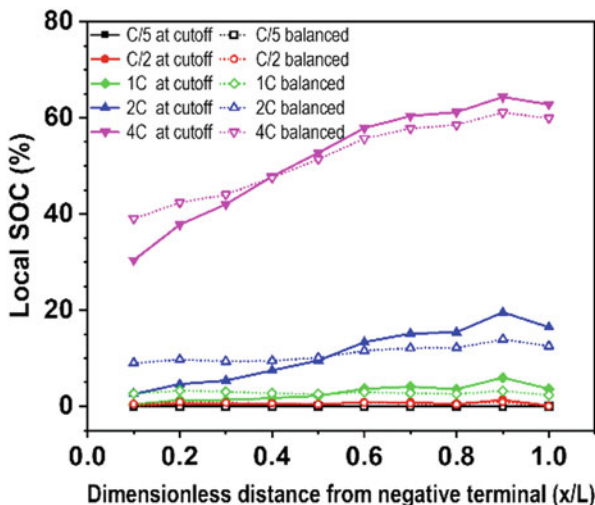


Fig. 2.14 Local SOC distribution in the experimental Li-ion cell before and after balancing

of the OCV-SOC curve at ~ 3.1 V (see Fig. 2.12), i.e., a small change in SOC is accompanied by a large change in OCV. Compare this observation with the resting after 4C discharge. As shown in Fig. 2.13b and magenta curves in Fig. 2.14, the cell remains at a significantly imbalanced after 3600 s of rest for 4C discharge, even though the voltage recovery rate (dV/dt) is as small as $0.5 \mu\text{V/s}$ at 3600 s. This behavior after 4C discharge can most likely be attributed to the shape of the OCV-SOC curve which has a significant slope between $\sim 20\%$ and 40% SOC but a much flatter slope between $\sim 40\%$ and 80% SOC. Therefore, significant SOC imbalance can be maintained in a Li-ion cell with LFP electrode if the local SOC distribution is the range with flat OCV. Indeed, the flat OCV-SOC behavior was previously used to freeze non-uniform SOC distribution in Li-ion cells with LFP cathode for ex situ measurement [50]. Consisting of lithium anode and LFP cathode, the cell was charged to 50% SOC, and then the LFP electrode was removed from the cell to be scanned by synchrotron X-ray microdiffraction. Significant non-uniformity of charge distribution was preserved and observed in the LFP electrode. Both the relatively lower currents of sections 5–10 (local SOC $> \sim 50\%$) in Fig. 2.13b, and the more significant recovery of SOC during rest for smaller (x/L) regions compared with the higher (x/L) sections, are also consistent with this argument.

These results imply that using nearly rested voltage as an indicator of cell internal balance may not be reliable. More specifically, the dV/dt tolerance to consider cell balancing may need to depend on the slope of the OCV-SOC curve in the region to which the voltage is resting. The recent battery excitation likely also plays a role in how appropriate a nearly rested voltage is in indicating a truly balanced battery. Further exploration of this phenomena is necessary.

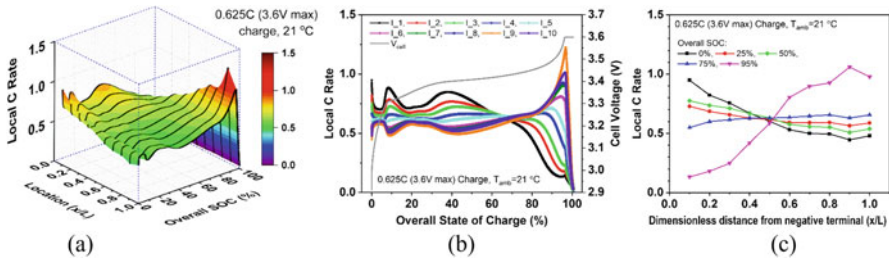


Fig. 2.15 Spatial-temporal current distribution during charging at 21 °C. (a) Variation of local currents with both location and overall SOC; (b) Variation of local currents and cell voltage with overall SOC; (c) Spatial current distribution at different overall SOC

2.2.2.7 Current Distribution During Charging

Figure 2.15 shows current distribution during charging at constant current of 1.5A, corresponding to 0.625C, followed by 3.6 V constant voltage charging until current drops to 0.02C. Due to change of charging current at constant voltage stage, local C rate is used to describe local currents. Similar to that during discharging, local current distribution is non-uniform during charging, especially at the beginning and end of constant current charging when cell voltage changes dramatically with SOC. Such non-uniform current distribution could dramatically exacerbate lithium plating during extreme fast charging that is actively pursued by EV industry. So further research on this would be particularly important. It is interesting to note that the trend of spatial current distribution is similar in both constant-current charging and discharging by comparing Figs. 2.5 and 2.15. At initial stages of charging or discharging, it is always segments closer to the negative terminal that experience higher local C rate. Since electrode materials degrade faster at higher C rate, it can be expected that such non-uniform current distribution could accelerate degradation of Li-ion cells.

2.2.2.8 Current Distribution During Partial Charging and Discharging

Li-ion cells in EV applications are not always fully charged or fully discharged. To investigate the effects of partial charging and discharging on current distribution, the experimental cell was cycled between 40% SOC and 60% SOC at 1C constant current three times. Before the cycling, the Li-ion cell was firstly fully charged, then discharged at C/5 to 60% SOC, followed by 1C discharge to 40% SOC, and then rest for 2 h. Figure 2.16 shows current distribution and cell voltage during such partial charging and discharging. Note that negative local C rate indicates the segments are charged. It can be seen that the current distribution behaviors are highly symmetrical during partial discharging and charging. Segments closer to the negative terminal always have higher local currents than those away from the negative terminal. For

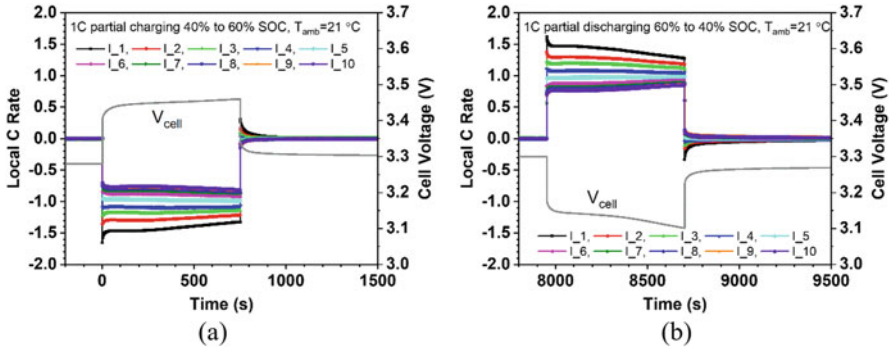


Fig. 2.16 Current distribution during partial charging and discharging cycling. (a) 1C charging from 40% SOC to 60% SOC; (b) 1C discharging from 60% SOC to 40% SOC

example, the local C rate of segment 1 ranges from 1.3 to 1.6, while that of segment 10 ranges only from 0.7 to 0.85. Even internal balancing currents are not enough to restore the non-uniformity. Such non-uniform current distribution and non-uniform material utilization would not only cause waste of material in locations far away from the tabs but also cause accelerated degradation of materials in locations closer to the tabs. Further investigation of how non-uniform current distribution influences degradation is needed to test this hypothesis.

2.2.2.9 Effects of Tab Configuration on Current Distribution and Usable Energy Density

Tab number and configurations have strong influence on performance of Li-ion batteries [14–15, 51]. But no quantitative relationship between cell energy density and current distribution was established experimentally in the literature. The EC Power-PSU team hypothesized that the effects of tab configurations on the energy density of Li-ion battery can be attributed to the effects on current distribution and experimentally validated the hypothesis.

Figure 2.17 shows schematically five tab configurations, all with the same negative tab but different positive tab configurations: ten positive tabs in parallel, five positive tabs in parallel, two positive tabs in parallel, one positive tab located counter to the negative tab, and one positive tab located at the same end of negative tab. When multiple positive electrode segments are connected in series, the additional resistance of positive tabs and shunt current sensors make the total resistance of positive current collector in this segmented cell much higher than that of a non-segmented cell. Therefore, the current distribution in this segment cell would be much more non-uniform than that in a non-segmented cell. It should be noted, however, that numerical models validated by the distribution data in this

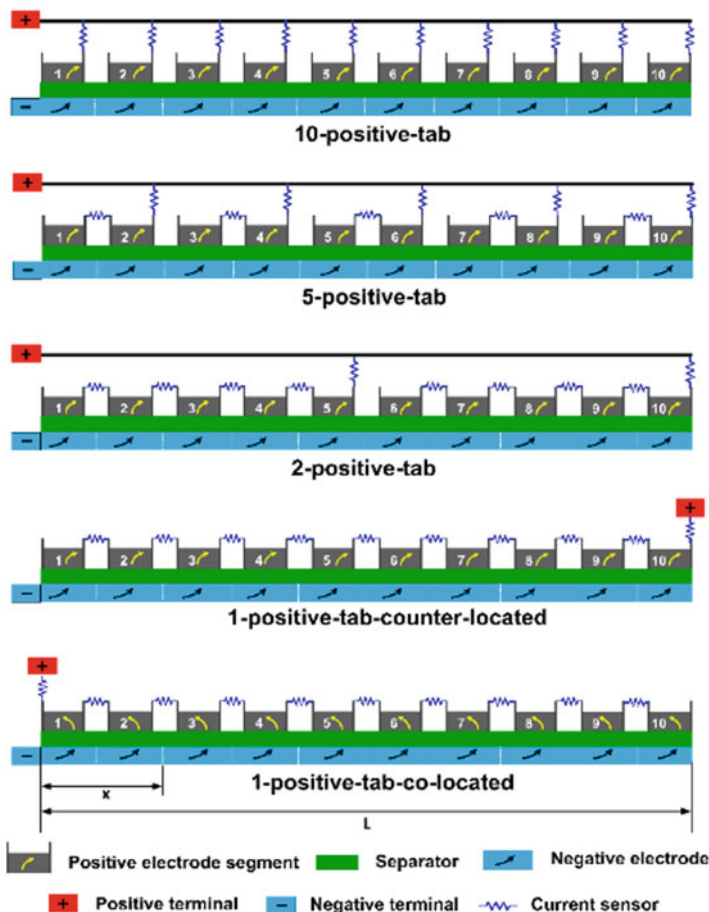


Fig. 2.17 Schematic of cell configurations with different positive tab numbers and locations. (Reused with permission from Ref. [28] Copyright 2013 The Electrochemical Society)

work can be used to explore various cases, including the case that both positive and negative electrodes are non-segmented.

Figure 2.18 shows overall performance of the experimental cell with different tab configurations. For convenience of comparison, the discharge capacity with 10-positive-tab configuration is used to calculate overall depth of discharge (DOD) for all the cases. Thus, the overall DOD in 10-tab case is set as 100%. As expected, tab number and location have significant effects on the overall performance of the experimental Li-ion cell. The cell voltage and discharge capacity are generally lower with fewer tabs, although the difference between 5-tab case and 10-tab case is very small. With same positive tab number, the 1-tab-co-located case has initially higher but then lower cell voltage than the 1-tab-counter-located case.

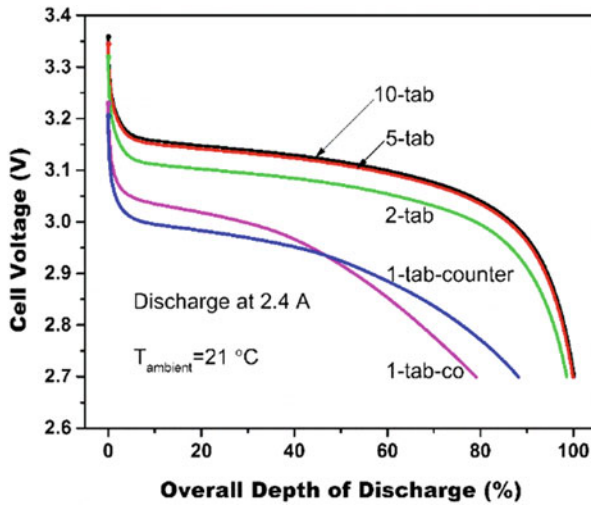


Fig. 2.18 Overall performance of the experimental Li-ion cell with different positive tab configurations. (Reused with permission from Ref. [28] Copyright 2013 The Electrochemical Society)

It is easy to understand that the generally lower cell performance with fewer tabs results directly from higher cell resistance. But the difference between 1-tab-counter-located case and 1-tab-co-located is not straightforward from overall performance comparison. Instead, it can be clearly explained by current distribution results in the two cases.

Figure 2.19 shows current distribution in the 1-tab-counter-located case. It can be seen that local current in segment 10 has the highest initial value and becomes

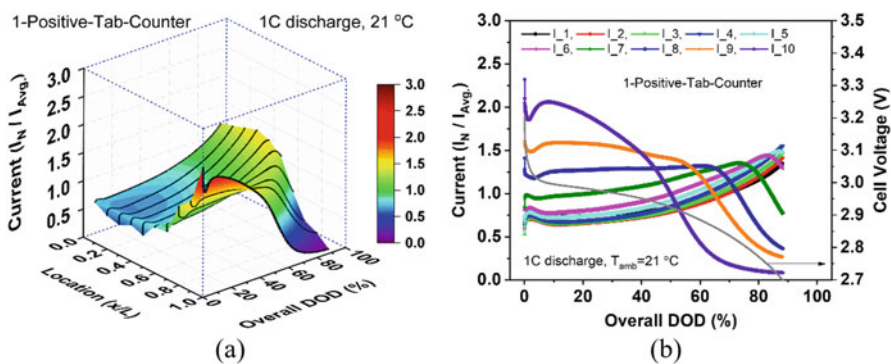


Fig. 2.19 Current distribution during discharge in 1-tab-counter-located configuration. (a) Variation of local currents with both location and overall SOC; (b) Variation of local currents and cell voltage with overall SOC. (Adapted with permission from Ref. [28] Copyright 2013 The Electrochemical Society)

lowest near the end of discharge. The non-uniform current distribution at beginning of discharge can be attributed to the effects of current collector resistance, especially the positive side. Local currents in segments 1–9 must flow through downstream segments, and the positive side resistance of downstream segments tends to make upstream local currents lower and downstream local currents higher. In this experimental cell, the resistance of current collector on positive side consists of segment aluminum foil resistance, segment tab resistance, and current sensor resistance, making positive side resistance higher than the negative side. As a result, the effects of positive side resistance on current distribution are dominant, and segment 10 generates the highest initial local current. Nevertheless, the counteracting effects of negative side current collector resistance can be still observed from the initial current distribution, in which segments 1 and 2 generate higher local currents than segment 3. Higher initial local current leads to faster depletion of active material. So the local current in segment 10, which has highest initial value, quickly depletes and becomes lowest. The depletion then propagates upstream as discharge proceeds.

Figure 2.20 shows current distribution in the 1-tab-co-located case. From comparison with Fig. 2.19, it can be seen that the current distribution in this case is almost opposite to that in the 1-tab-counter-located case, and the current distribution is even less uniform. Difference of current distribution in the two cases can be attributed to how the effects of positive current collector resistance and negative current collector resistance interact. As discussed above, in the 1-tab-counter-located case, the effects of positive side resistance and negative side resistance are counteracting. In the 1-tab-co-located case, however, the effects are synergizing, both favoring higher local currents in upstream segments. Therefore, in the 1-tab-co-locate case, the local current in segment 1 is exceptionally high and that in segment 10 exceptionally low during initial period of discharge. As discharge

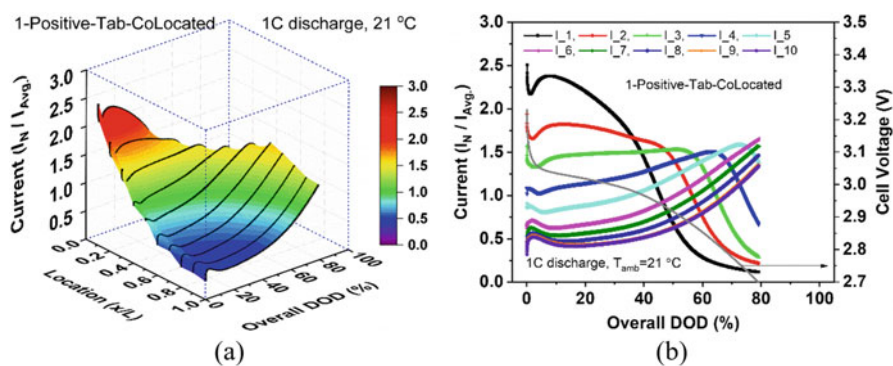


Fig. 2.20 Current distribution during discharge in 1-tab-co-located case. (a) Variation of local currents with both location and overall SOC; (b) Variation of local currents and cell voltage with overall SOC. (Adapted with permission from Ref. [28] Copyright 2013 The Electrochemical Society)

proceeds, the stored energy in segment 1 is more quickly depleted, and the local current quickly becomes the lowest.

With detailed results of current distribution in the 1-tab-co-located case and the 1-tab-counter-located case, the difference of overall cell performance shown in Fig. 2.17 can be clearly explained. Initially, a great portion of total current is generated in upstream segments in the 1-tab-co-located case, while the situation is opposite in the 1-tab-counter-located case. So the average travel distance of local currents through the positive and negative and current collectors is much shorter in the 1-tab-co-located case. Consequently, the average resistance is lower. With the battery cell discharged at the same total current, the voltage drop is lower in 1-tab-co-located case, resulting in increased utilization. As discharge proceeds, however, stored energy in upstream segments is depleted quickly due to very high initial local currents. As the depletion moves downstream, reactions in downstream segments are accelerated to keep the total current constant. As a result, the average travel distance of the total current becomes longer, with the average resistance and voltage drop becoming higher. The variation of current distribution, the average travel distance of total current, and the average resistance is essentially opposite in the 1-tab-counter-located case. Therefore, the difference of cell voltage between the two cases becomes smaller as the discharge proceeds. Eventually the cell voltage in the 1-tab-co-located case becomes equal to, and then lower than, that in the 1-tab-counter-located case.

The very non-uniform current distribution in 1-tab-co-located case suggests two potential problems. First, energy storage materials in downstream segments are significantly underutilized, leading to reduced energy density, an undesired waste. Second, electrodes closer to tabs produce higher local currents (higher C rate) than average and experience faster depletion during discharge, even overdischarge of active materials. Previous studies showed that a Li-ion cell degrades faster for higher C rate and higher DOD [52–53], so electrode materials near tabs are likely to degrade faster, eventually causing the whole cell to degrade faster than a cell with uniform current distribution. Therefore, improving current distribution in Li-ion cells through design optimization is beneficial for energy density and durability, both of which are major challenges for electric vehicle applications. Correlating current distribution non-uniformity with degradation through in situ measurement of current distribution in aging tests can provide more insights about large-format Li-ion cell degradation. Further research efforts along these directions are warranted.

The non-uniform utilization of active materials in 1-tab-co-located case is further demonstrated in Fig. 2.21, in which DOD distributions at cutoff in different cases are compared. It can be seen that the DOD distribution in the 10-tab and 5-tab cases are very similar and rather uniform, with only downstream segments slightly underutilized. In comparison, some segments are much less utilized in other cases depending on the tab configuration, particularly in the 1-tab-co-located and 1-tab-counter-located cases. It is interesting to note that local DOD of upstream segments in the 1-tab-co-located case is very similar to the 10-tab case and 5-tab case, while that of downstream segments is much lower. This clearly shows the effects of current distribution on energy utilization of Li-ion cell.

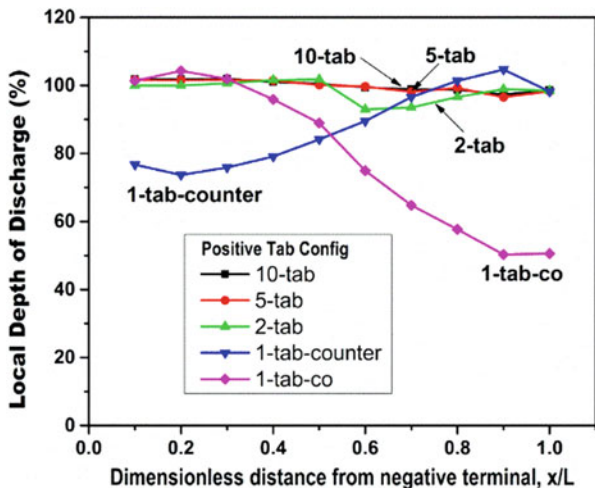


Fig. 2.21 Comparison of local DOD distribution at cutoff with different tab configurations. (Reused with permission from Ref. [28] Copyright 2013 The Electrochemical Society)

The very similar overall performance, current distribution, and DOD distribution in 5-tab case and 10-tab case suggests that excessive tab number helps little. Actually, excessive tabs increase the complexity and cost of battery cell manufacturing, which is not desired.

2.2.2.10 Correlation Between Energy Density and Current Distribution Non-uniformity

The current distribution and DOD distribution results in Fig. 2.21 indicate that non-uniform current distribution lead to underutilization of active materials and lower energy density. To establish the correlation between non-uniform current distribution and energy density more clearly, discharge energy is plotted as a function of current distribution non-uniformity factor [15] in Fig. 2.22. Discharge energy is normalized by that during C/5 discharge with 10-tab configuration, which is assumed to be the maximum energy available from the experimental cell. It can be seen that the normalized energy decreases almost linearly with the increase of current distribution non-uniformity factor. It demonstrates a significant effect of current distribution non-uniformity on energy density and the importance of improving current distribution uniformity in energy-dense Li-ion batteries for vehicle energy storage.

The experimental correlation between usable energy density and current distribution non-uniformity results was later used by Zhao et al. [15] to validate numerical models. As shown in Fig. 2.23, the model results of 40 Ah Li-ion cells were superimposed with the experimental data of the 2.4 Ah LFP/graphite cell. The

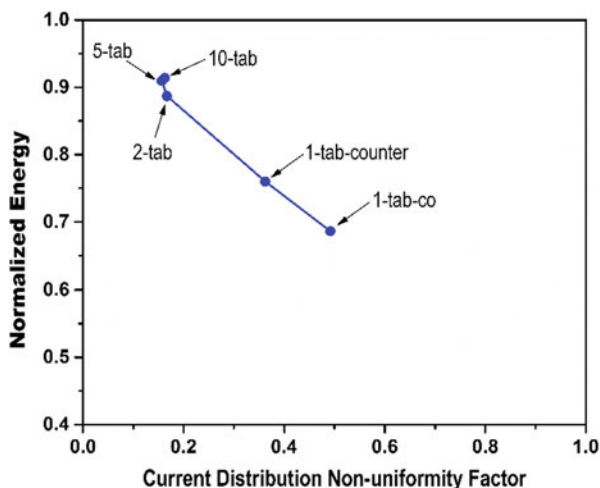


Fig. 2.22 Normalized discharge energy vs. current distribution non-uniformity factor. (Reused with permission from Ref. [28] Copyright 2013 The Electrochemical Society)

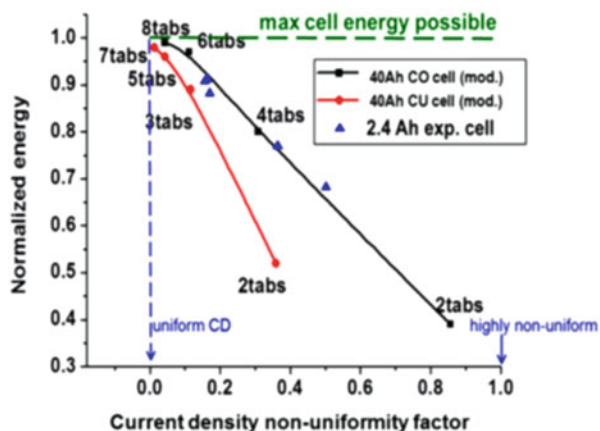


Fig. 2.23 Comparison of modeling results for 40 Ah cells by Zhao et al. [15] with experimental data for 2.4 Ah segmented Li-ion cell. (Reused with permission from Ref. [15] Copyright 2014 Elsevier B.V)

energy density was for 1 C discharge process and was normalized by the coin cell energy density, i.e., the maximum achievable energy density with the battery materials used. Despite differences in size and cathode material, the trend and magnitude of cell energy density vs. current density non-uniformity are clearly consistent between the model predictions and experiments. More quantitative comparisons using the NMC chemistry and the exact cell size need to be carried out in the future.

2.3 Indirect Diagnosis of Current Distribution Through Local Potential Measurement

As schematically shown in Fig. 2.1, when current flows in copper foil and aluminum foil current collectors, there will be electric potential change along the length of current collectors due to ohmic resistance. By measuring distribution of local potential along the foils, it is possible to estimate local currents through numerical models. A team at Technical University of Munich (TUM) and their collaborators [31–33] took this approach, firstly using a modified commercial cylindrical cell [31–32] and then using a specially developed single-layered pouch cell [33]. The team's work is reviewed in this section.

2.3.1 *Experimental Method Using Modified Commercial Cylindrical Cells*

Figures 2.24 and 2.25 show schematic and pictures of cylindrical cell before and after modification by Osswald et al. [31]. Before modification, there are four parallel connected tabs on negative electrode (A1–A4) and four parallel connected tabs on positive electrode (C1–C4). External current is applied to the cell through all the tabs, and only one voltage can be measured. After modification, the four tabs on each electrode are separated. External current is applied only through one pair of tables (A1 and C1) in the study, creating a co-located tab configuration which would create more non-uniform current distribution than other tab configurations [15, 28]. The modification allows for voltage measurements at four different positions of the electrode, which are used to validate models and simulation of local current densities [32].

The cylindrical cells used for modification purposes are commercially available 26650 format cells with a nominal capacity of 2.5 Ah and an average discharge voltage of 3.3 V. The cathode has an overall length of 1.69 m, the anode 1.75 m, and each electrode has four almost equidistant current collecting tabs. The aluminum current collector is 20 μm thick, and the copper current collector is 13 μm thick. Lithium iron phosphate is used for the cathode's active material, and graphite is used for the anode. More experimental details are also reported [31].

2.3.2 *Results from Modified Commercial Cylindrical Cell*

Figure 2.26 shows measured and simulated voltages at each of the four tab pairs of the modified cell during 0.5C, 1C, and 2C discharge at room temperature. It can be seen that local voltage measured at tab 1 is significantly lower than those at other locations and the difference increased at higher C rate. The results clearly

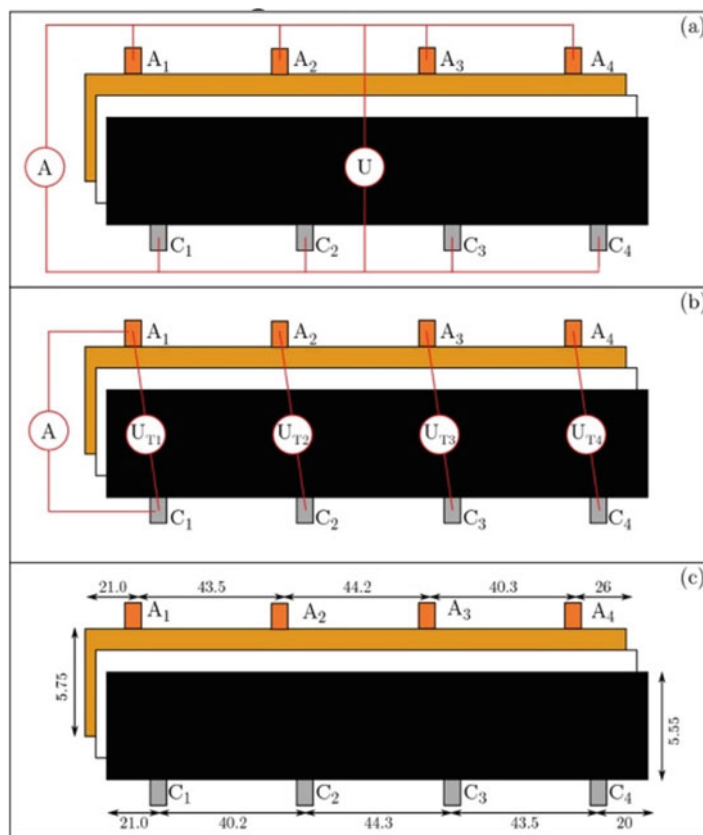


Fig. 2.24 Schematic and operation mode of experimental cell by Osswald et al. [31]. (a) Before modification all four tabs on each electrode (A1–A4 on negative electrode and C1–C4 on positive electrode) are connected in parallel and applied external current; (b) After modification tabs are separated, allowing voltage measurements at four different positions, and only outermost pair of tabs (A1 and C1) is applied external current; (c) Locations of tabs. (Reused with permission from Ref. [31] Copyright 2015 The Electrochemical Society)

demonstrated the effects of current collector resistance on local voltage distribution, which would influence current distribution. Note that when tab 1 voltage reached cutoff value of 2.4 V at the end of 2C discharge, other tab voltages are still 2.8 V and above, suggesting underutilization of capacity in regions farther away from terminals [32], consistent with the EC Power-PSU team’s findings on co-located tab configuration [15, 28].

Figure 2.27 shows simulated current density in electrodes at each of the four tab pairs corresponding to the voltage results in Fig. 2.25. It can be seen that the trend of current distribution is consistent and similar to that measured by the EC Power-PSU team with co-located tab configuration. Local current densities in region closest to terminals are highest at beginning of discharge but quickly decrease due to depletion

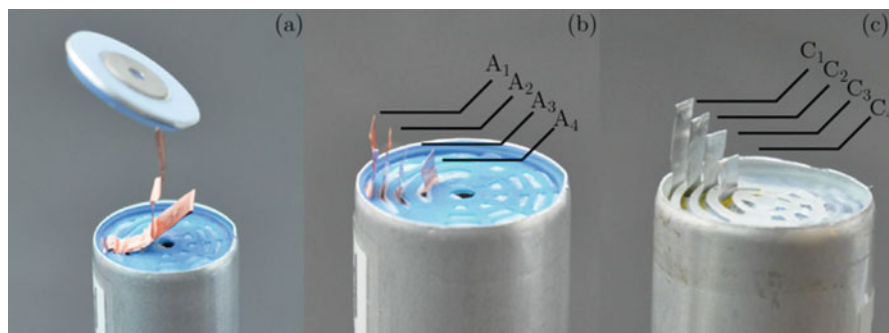


Fig. 2.25 Pictures of experimental cell by Osswald et al. [31] (a) Opened on the negative electrode with four tabs connected; (b) Opened on the negative end with current tabs separated; (c) Opened on the positive electrode with current tabs separated. (Reused with permission from Ref. [31] Copyright 2015 The Electrochemical Society)

of local SOC. Then local current densities in regions further away from the terminals increase correspondingly and then also decrease due to depletion of SOC. Such a distinct trend is governed by the same mechanism, i.e., nonlinear decrease of local open circuit voltage with SOC, primarily from the graphite anode.

2.3.3 *Experimental Method Using Single-Layered Pouch Li-Ion Cell*

As shown in Fig. 2.28, Erhard et al. [33] developed a single-layered pouch cell with ten tab pairs at each edge for potential distribution measurement. There is also a reference tab pair at the left and right side of the cell to be connected to battery tester. The current collectors are 500 mm long and 100 mm wide. The aluminum current collector is 20 μm thick, and the copper current collector is 18 μm thick. Compared with the segmented pouch cell by the EC Power-PSU team and the cylindrical cell used by the same TUM team, the length of current collector in this work is much shorter but still comparable to large-format pouch cells in which electrodes are stacked instead of being wounded. The copper foil in this work is thicker than normally used which could influence current distribution behaviors. A unique feature of this experimental cell is single-layered structure, which can dramatically reduce effects of non-uniform temperature distribution and heat generation on current distribution as experienced in the large cylindrical cell [32].

The cell comprises a $\text{LiNi}_{0.33}\text{Mn}_{0.33}\text{Co}_{0.33}\text{O}_2$ (NMC) cathode and a graphite anode with nominal capacity of 0.8 Ah. NMC is increasingly used in EV applications, and its open circuit potential behavior is different from LFP cathode, which would influence current distribution behaviors.

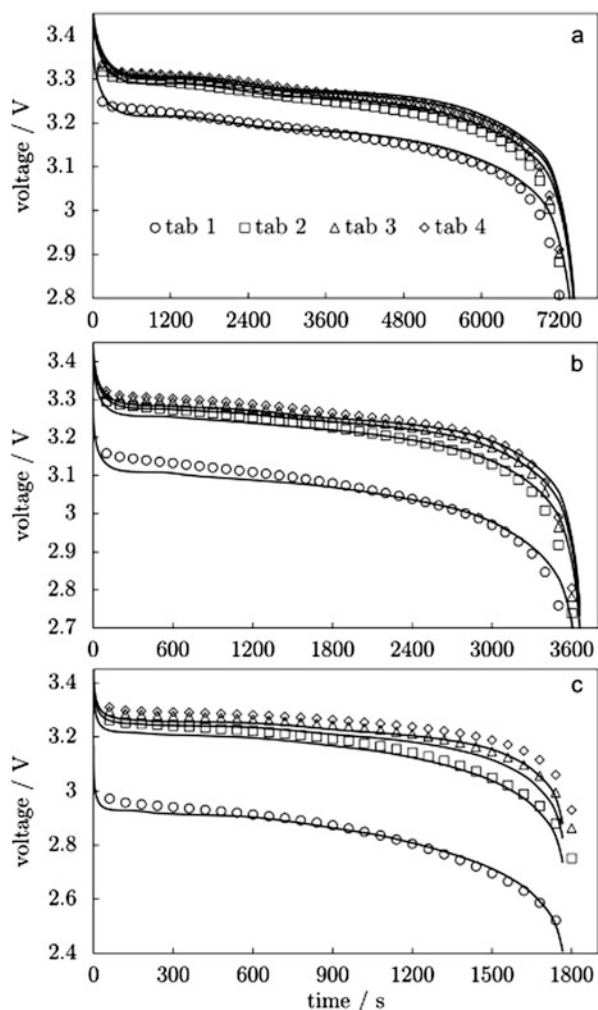


Fig. 2.26 Measured and simulated voltages across each of the four tab pairs during (a) 0.5C, (b) 1C, and (c) 2C discharge at room temperature. (Reused with permission from Ref. [32] Copyright 2015 The Electrochemical Society)

Figure 2.29 shows schematically the team's experimental setup [33]. In their study, the current from the battery tester was only applied at one of the two reference tab pairs, creating a co-located tab configuration similar to that in their work on cylindrical cell. This tab configuration would create more non-uniform current distribution than other configurations, and it is not advised for actual application [15, 28]. A climate chamber was used to control ambient temperature.

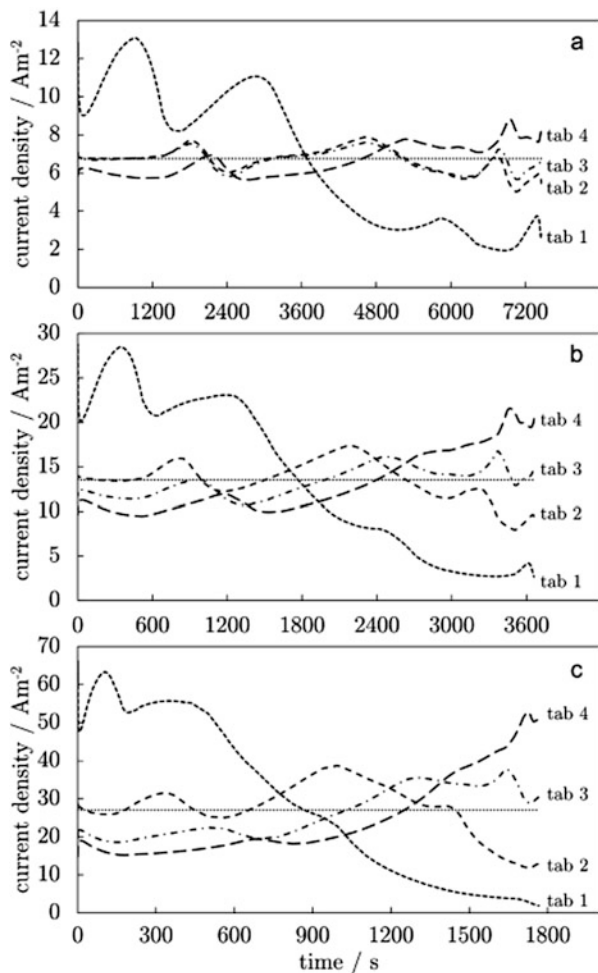


Fig. 2.27 Simulated current density in electrodes at each of the four tab pairs during (a) 0.5C, (b) 1C, and (c) 2C discharge at room temperature. (Reused with permission from Ref. [32] Copyright 2015 The Electrochemical Society)

2.3.4 Results from Single-Layered Pouch Li-Ion Cell

Figure 2.30 shows experimental and simulation results during 0.5C, 1C, and 2C discharge at a temperature of 25 °C by Erhard et al. [33]. It can be seen that the wavy current distribution behaviors are similar to the results reported by the EC Power-PSU team [27], suggesting similar controlling mechanism of current distributions in Li-ion cells despite different electrode materials. Local measurement point #01 is much closer to the terminals (reference tabs) than measurement point #10, so the resistance is lower, causing higher local current at point #01 than that at #10 at initial

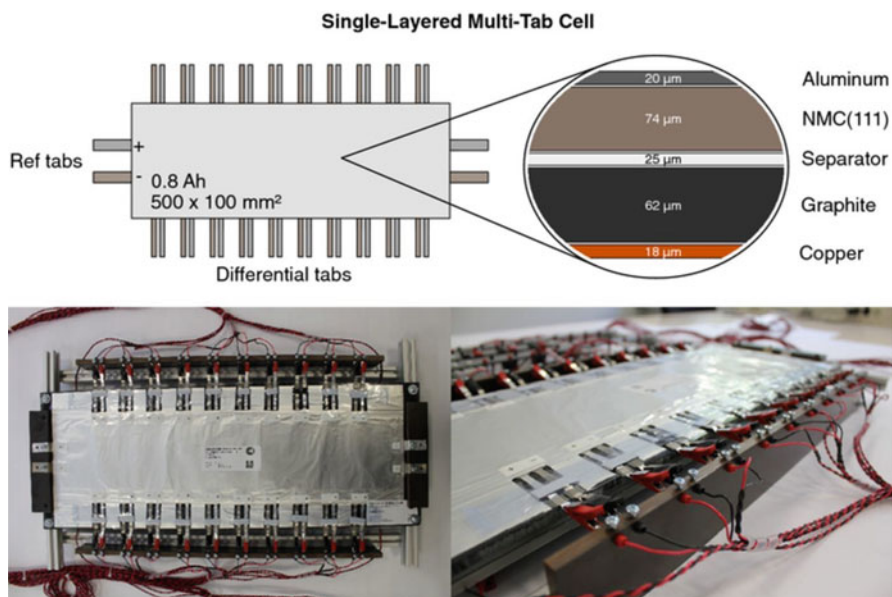


Fig. 2.28 Schematic representation and pictures of a single-layered pouch Li-ion cell for potential distribution measurement by Erhard et al. [33]. (Reused under the terms of the Creative Commons Attribution 4.0 License (CC BY) from Ref. [33] Copyright 2017 The Authors. Published by ECS)

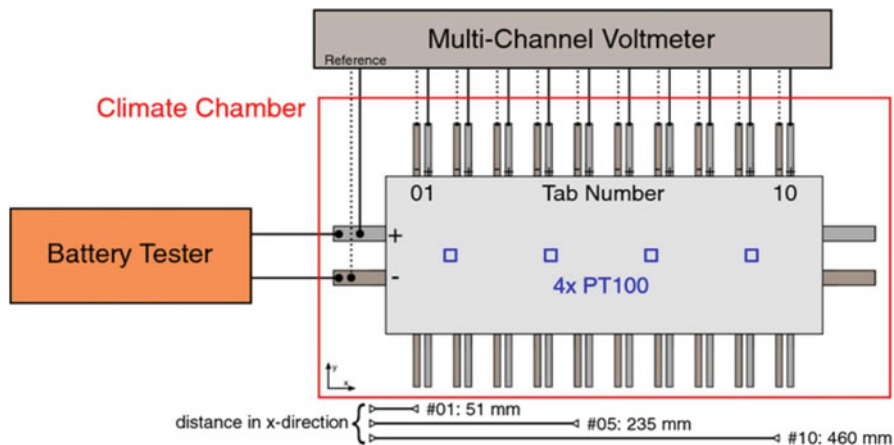


Fig. 2.29 Schematic representation of experimental setup for potential distribution measurement by Erhard et al. [33]. (Reused under the terms of the Creative Commons Attribution 4.0 License (CC BY) from Ref. [33] Copyright 2017 The Authors. Published by ECS)

stages of discharge. As discharging proceeds, local SOC and therefore local OCV would cause the current distribution to reverse near the end of discharge. The local current curves are less wavy during 2C discharge than during 0.5C discharge, also

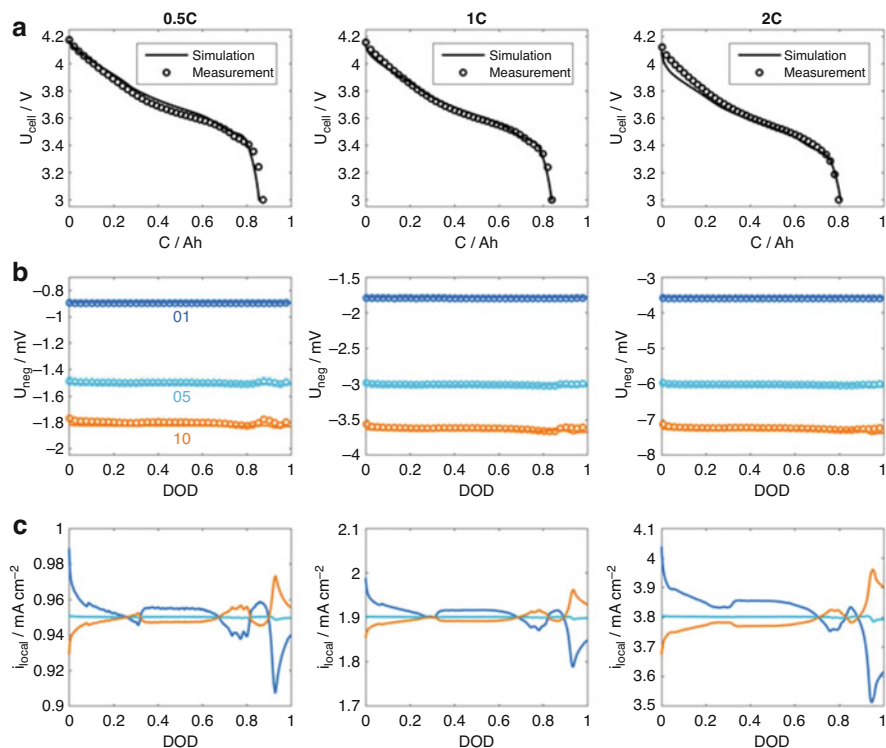


Fig. 2.30 Experimental and simulation results during 0.5C, 1C, and 2C discharge at a temperature of 25 °C by Erhard et al. [33]. (a) Measured (symbols) and simulated (solid lines) cell voltage; (b) Measured and simulated potentials at local measurement points #01, #05, and #10; (c) Simulated current densities at the corresponding points. (Reused under the terms of the Creative Commons Attribution 4.0 License (CC BY) from Ref. [33] Copyright 2017 The Authors. Published by ECS)

consistent with the results reported by the EC Power-PSU team [27] on the effects of discharging C rate.

Figure 2.31 shows experimental and simulation results during 1C discharge at temperatures of 5 °C, 25 °C and 40 °C by Erhard et al. [33]. Current distributions are more non-uniform and wavy at higher temperatures which could be attributed to the change of reaction kinetics and cell resistance at different temperatures.

Erhard et al. [33] also simulated local SOC distribution during discharge. Figure 2.32 shows simulated difference in SOC between tab #01 and tab #10 during 0.5C, 1C, and 2C discharge at 25 °C. As expected, the difference initially increased due to difference in local currents but eventually reduced near the end of discharge due to reverse of current distribution trend. The difference is more significant at higher C rate and higher temperature, also corresponding to the behaviors of current distribution. It is interesting to note that the SOC difference at end of 2C discharge is much smaller than that reported by the EC Power-PSU team [27], which can be

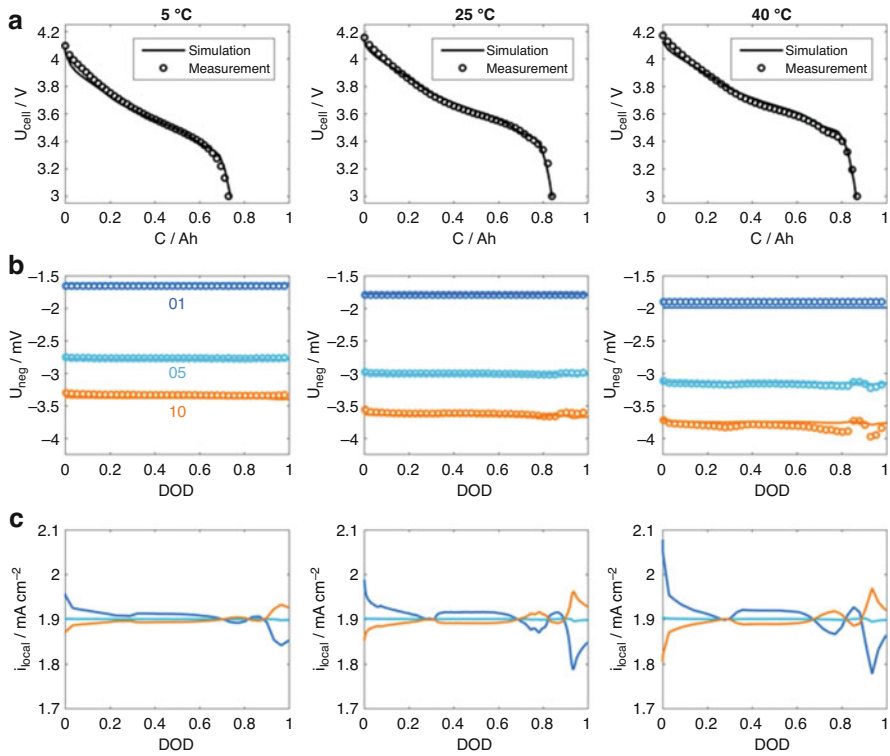


Fig. 2.31 Experimental and simulation results during 1C discharge at temperatures of 5 °C, 25 °C and 40 °C by Erhard et al. [33]. (a) Measured (symbols) and simulated (solid lines) cell voltage; (b) Measured and simulated potentials at local measurement points #01, #05, and #10; (c) Simulated current densities at the corresponding points. (Reused under the terms of the Creative Commons Attribution 4.0 License (CC BY) from Ref. [33] Copyright 2017 The Authors. Published by ECS)

attributed to difference between NMC cathode and LFP cathode in dependence of open circuit potential on SOC. The difference would be more dramatic at higher C rate and is worth further investigation.

2.4 Noninvasive Diagnosis of Current Distribution Using Magnetic Resonance Imaging

A magnetic field is generated as electric current flows in a Li-ion cell. By mapping the generated magnetic field using magnetic resonance imaging techniques, it is possible to noninvasively detect current flow inside Li-ion cells. A team at New York University recently demonstrated this concept [34]. In an earlier work, the

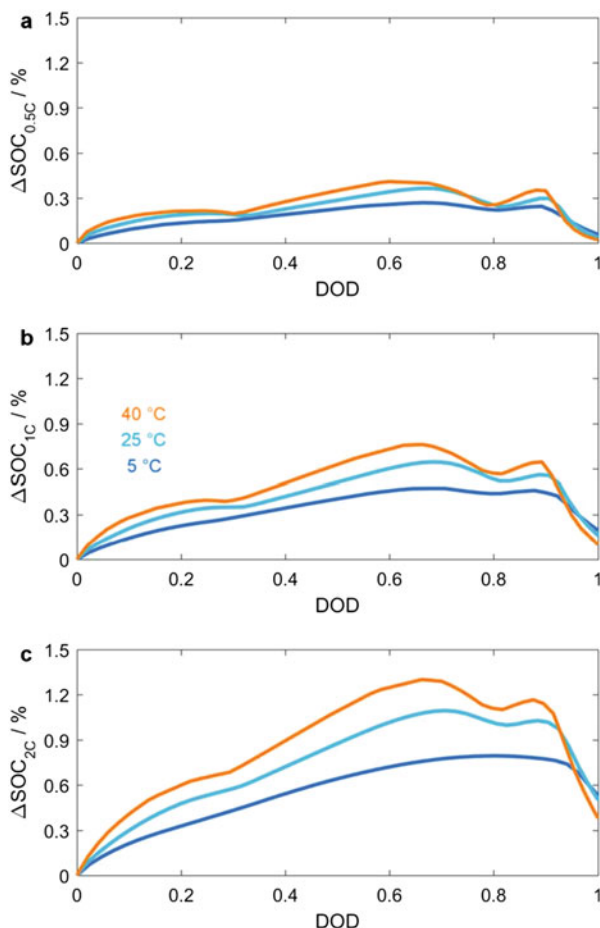


Fig. 2.32 Simulated difference in SOC between tab #01 and tab #10 during 0.5C, 1C, and 2C discharge at 25 °C [33]. (Reused under the terms of the Creative Commons Attribution 4.0 License (CC BY) from Ref. [33] Copyright 2017 The Authors. Published by ECS)

team and their collaborators demonstrated the use of magnetic resonance imaging to noninvasively determine Li-ion cell state of charge [54].

2.4.1 Measurement Method Using Magnetic Resonance Imaging

Figure 2.33a shows an illustration of the experimental arrangement by Mohammadi et al. [34]. A pouch-type Li-ion cell is placed in a customer-designed holder

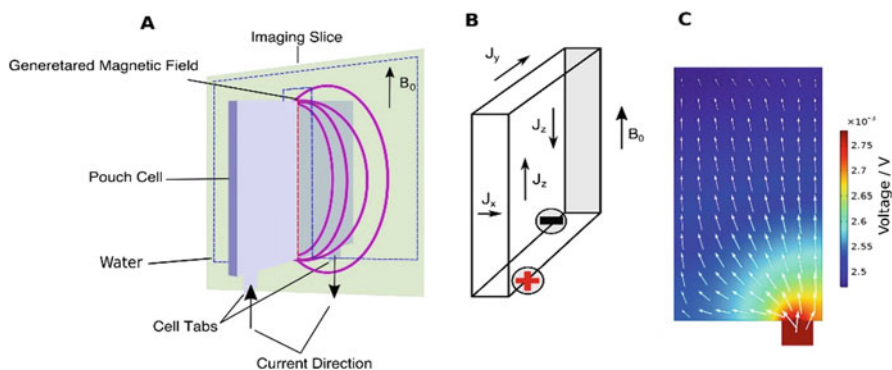


Fig. 2.33 Illustration of the experimental arrangement by Mohammadi et al. [34]. (a) Cell position and orientation of imaging slice, with dashed rectangle indicating detected volume; (b) Directions of current flow and cell orientation; (c) Calculated current and voltage distribution on the positive current collector during charging. (Reused with permission from Ref. [34] Copyright 2019 Elsevier Inc.)

containing water compartments that sandwiching the Li-ion cell. 15 mM CuSO_4 water solution is filled in the compartments as detection medium. A strong external static magnetic field B_0 is applied along z direction (from cell end with tabs to the opposite end). Then the magnetic field generated by current flowing along y direction (J_y in Fig. 2.33b) is detected by comparing magnetic field maps with current flow and at rest. As shown in Fig. 2.33c, the authors also calculated current distribution in positive current collector during charging, but the calculation seemed to be based on a simplified electric model and not based on measured magnetic field data.

2.4.2 Results from Magnetic Resonance Imaging

Mohammadi et al. [34] demonstrated the technique using Li-ion pouch cells with capacity of 250 mAh. Each cell was composed of five double-sided cathodes and six double-sided anodes. The active materials in cathode and anode were $\text{Li}_{1.02}\text{Ni}_{0.50}\text{Mn}_{0.29}\text{Co}_{0.19}\text{O}_2$ and graphite, respectively. The electrolyte was 1.2 M LiPF_6 in EC:DMC 3:7 (%wt). Figure 2.34 shows magnetic field maps and histograms during discharge and charge at the imaging slice indicated by the dashed rectangle in Fig. 2.33a. Negative current indicates discharging and positive current indicates charging. The magnetic field maps were obtained after subtracting a reference image from resting period and a constant background field. Red color indicates positive change of magnetic field, and blue color indicates negative change of magnetic field. The discharge or charge current was 125 mA, corresponding to 0.5C. The results show the influence of internal current flow on the magnetic field.

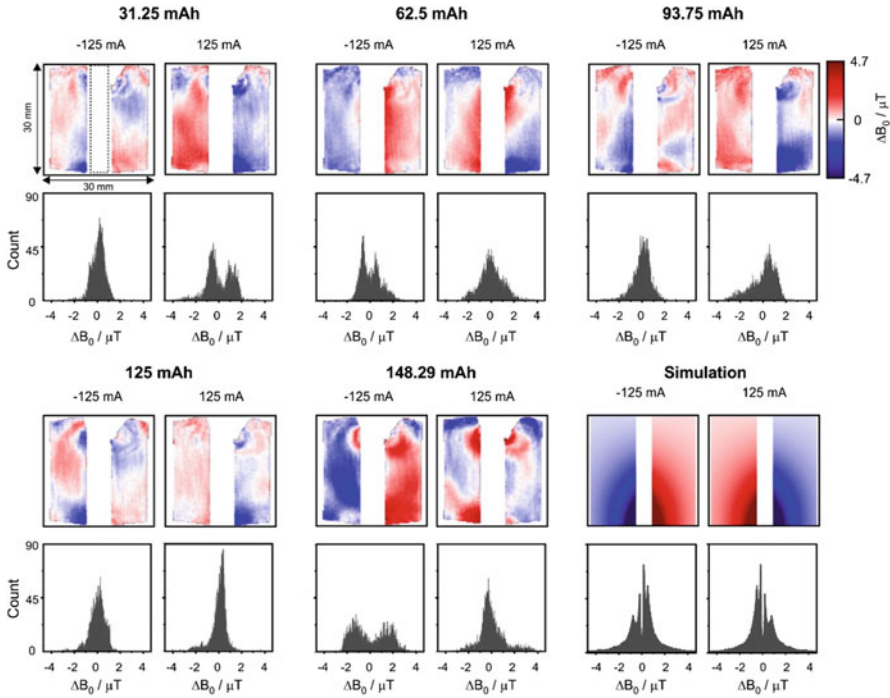


Fig. 2.34 Magnetic field maps and histograms during discharge (negative current) and charge (positive current) at different depth of discharge as indicated. The battery tabs in these measurements are located at the bottom of each map. The imaging dimensions and the location of the cell (dotted rectangle) are indicated in the top left image. (Reused with permission from Ref. [34] Copyright 2019 Elsevier Inc.)

It can be seen that the changes of magnetic field depend on direction of current and depth of discharge, which could be used to detect existence of current flow or even local current distribution. However, quantified current distribution from measured magnetic field was not reported. The study also examined correlation of magnetic field with applied current and found significant deviation from linearity. Further work would be needed to quantify current distribution from magnetic resonance imaging.

2.5 Summary and Future Work

As reviewed above, non-uniform distribution in large-format Li-ion cells has significant negative influences in power performance, usable energy density, durability, and safety, which are critical to EV applications. Novel techniques, including segmented cells, cells with embedded potential sensors, and noninvasive imag-

ing, have been demonstrated as effective tools for in situ diagnosis of current distribution. Moreover, insights on Li-ion cells were obtained through spatial-temporal distribution of current densities that could not be obtained from overall cell performance characterization. In particular, the non-uniform and wavy distribution of local currents are experimentally found. The effects of non-uniform current distribution on underutilization of active materials, internal balancing current, and its influence on SOC redistribution and cell voltage recovery were observed. The effects of tab configuration on current distribution and thus usable energy density were revealed. Experimental spatial-temporal data are also important in validating multidimensional electrochemical-thermal coupled models that are increasingly used for Li-ion battery development.

With the widespread adoption of electric vehicles around the globe, which increasingly demands for Li-ion batteries with higher material utilization, further efforts are needed in diagnosing current distribution in large-format Li-ion cells for insights to develop faster rechargeable, more energy dense, safer, and more durable Li-ion batteries. Here we propose a few topics that are particularly worth investigating from EV battery perspective.

The first suggested topic is measurement of current distribution under extreme conditions such as extreme fast charging, extreme thermal conditions (as low as $-40\text{ }^{\circ}\text{C}$ and as high as $80\text{ }^{\circ}\text{C}$), and safety abuse conditions (mechanical puncture, crash, or internal short circuit). Lithium plating is a critical challenge for fast charging [55], and it can be exacerbated by non-uniform current distribution. Under extreme low temperatures and rapid heating process, the internal resistance of Li-ion cells changes dramatically, which would cause dramatic change of current distribution. Under safety abuse conditions, the current distribution would be extremely non-uniform and dynamically changing [25, 56]. In situ measurement of current distribution under these extreme yet important conditions would help achieve better understanding and development of Li-ion cells that perform better and more safely.

The second suggested topic is measurement of current distribution in Li-ion cells during long-term or accelerated aging. A recent study by Cavalheiro et al. [37] showed that current distribution in a small module consisting of parallel-connected Li-ion cells greatly varied during aging and contributed to accelerated aging. A similar mechanism is expected to exist at the cell level and worth further investigation for large-size cells. The effects of cooling conditions, cell constraint, and compression on current density distribution and failure are also necessary.

The third suggested topic is measurement of current distribution in Li-ion cells with emerging materials, such as low cobalt cathode, silicon-based anode, or solid-state electrolytes. Current distribution behaviors of cells with these materials could be very different as implied by the comparison of studies with LFP cathode [27] and NMC cathode [33]. In particular, silicon anode [57] and low cobalt NMC cathode [58] degrade faster than conventional electrode materials. The interaction between degradation and current distribution is worth investigation.

The last but not the least suggested topic is development of new methods for current distribution diagnosis in large-format EV Li-ion cells. While the reported

methods revealed many interesting phenomena, each has its own disadvantages. The segmented cell method enables direct measurement of current distribution, but it requires significant modification of Li-ion cells. Indirect measurement with embedded potential sensors requires less modification, but calculating current distribution from potential distribution requires thermal-electrochemical modeling. Noninvasive diagnosis through magnetic resonance does not require any modification of experimental cells, but quantification of current distribution from magnetic field map and its application to extreme conditions could be challenging. Moreover, the reported current distributions are primarily one dimensional. It would be necessary to extend the measurement to two dimensional or three dimensional for comprehensive understanding of the behaviors in a large-format EV Li-ion cells with capacity of more than 100 Ah. It would be also valuable to integrate the current distribution diagnosis with other in situ diagnostic tools, such as in situ temperature distribution measurement [29, 56, 59–61], in situ neutron imaging [62], and X-ray methods [63–64].

References

1. Whittingham MS (2012) History, evolution, and future status of energy storage. *Proc IEEE* 100(Special Centennial Issue):1518–1534
2. Winter M, Barnett B, Xu K (2018) Before Li ion batteries. *Chem Rev* 118(23):11433–11456
3. Bloomberg New Energy Finance (2020) Electric vehicle outlook 2020. <https://about.bnef.com/electric-vehicle-outlook/>
4. DOE Office of Science (2017) Report of basic research needs workshop on next generation electric energy storage. https://science.energy.gov/~media/bes/pdf/reports/2017/BRN_NGEES_rpt.pdf
5. DOE (2020) 2020 Annual merit review report. <https://www.energy.gov/eere/vehicles/downloads/2020-annual-merit-review-report>
6. Ahmed S, Bloom I, Jansen AN, Tanim T, Dufek EJ, Pesaran A, Burnham A, Carlson RB, Dias F, Hardy K, Keyser M, Kreuzer C, Markel A, Meintz A, Michelbacher C, Mohanpurkar M, Nelson PA, Robertson DC, Scofield D, Shirk M, Stephens T, Vijayagopal R, Zhang J (2017) Enabling fast charging – a battery technology gap assessment. *J Power Sources* 367(Supplement C):250–262
7. Wang C-Y, Xu T, Ge S, Zhang G, Yang X-G, Ji Y (2016) A fast rechargeable lithium-ion battery at subfreezing temperatures. *J Electrochem Soc* 163(9):A1944–A1950
8. Yang X-G, Zhang G, Ge S, Wang C-Y (2018) Fast charging of lithium-ion batteries at all temperatures. *Proc Natl Acad Sci* 115(28):7266–7271
9. Yang X-G, Liu T, Gao Y, Ge S, Leng Y, Wang D, Wang C-Y (2019) Asymmetric temperature modulation for extreme fast charging of lithium-ion batteries. *Joule* 3(12):3002–3019
10. Wang C-Y, Zhang G, Ge S, Xu T, Ji Y, Yang X-G, Leng Y (2016) Lithium-ion battery structure that self-heats at low temperatures. *Nature* 529(7587):515–518
11. Feng X, Ouyang M, Liu X, Lu L, Xia Y, He X Thermal runaway mechanism of lithium ion battery for electric vehicles: a review. *Energy Storage Mater* 2018, 10:246–267
12. Ruiz V, Pfrang A, Kriston A, Omar N, Van den Bossche P, Boon-Brett L (2018) A review of international abuse testing standards and regulations for lithium ion batteries in electric and hybrid electric vehicles. *Renew Sust Energ Rev* 81:1427–1452
13. Sun P, Bisschop R, Niu H, Huang X (2020) A review of battery fires in electric vehicles. *Fire Technol* 56(4):1361–1410

14. Lee K-J, Smith K, Pesaran A, Kim G-H (2013) Three dimensional thermal-, electrical-, and electrochemical-coupled model for cylindrical wound large format lithium-ion batteries. *J Power Sources* 241:20–32
15. Zhao W, Luo G, Wang C-Y (2014) Effect of tab design on large-format Li-ion cell performance. *J Power Sources* 257:70–79
16. Doyle M, Fuller TF, Newman J (1993) Modeling of galvanostatic charge and discharge of the lithium/polymer/insertion cell. *J Electrochem Soc* 140(6):1526–1533
17. Smith K, Wang C-Y (2006) Power and thermal characterization of a lithium-ion battery pack for hybrid-electric vehicles. *J Power Sources* 160:662–673
18. Smith K, Wang C-Y (2006) Solid-state diffusion limitations on pulse operation of a lithium ion cell for hybrid electric vehicles. *J Power Sources* 161:628–639
19. Ramadesigan V, Methekar RN, Latinwo F, Braatz RD, Subramanian VR (2010) Optimal porosity distribution for minimized ohmic drop across a porous electrode. *J Electrochem Soc* 157(12):A1328–A1334
20. Santhanagopalan S, Guo Q, Ramadass P, White RE (2006) Review of models for predicting the cycling performance of lithium ion batteries. *J Power Sources* 156(2):620–628
21. Ramadesigan V, Northrop PWC, De S, Santhanagopalan S, Braatz RD, Subramanian VR (2012) Modeling and simulation of lithium-ion batteries from a systems engineering perspective. *J Electrochem Soc* 159(3):R31–R45
22. Fang W, Kwon OJ, Wang C-Y (2010) Electrochemical-thermal modeling of automotive Li-ion batteries and experimental validation using a three-electrode cell. *Int J Energy Res* 34:107–115
23. Luo G, Wang CY (2012) A multidimensional, electrochemical-thermal coupled lithium-ion battery model, Chapter 7. In: Yuan X, Liu H, Zhang J (eds) *Lithium-ion batteries*. CRC Press, Boca Raton
24. Zhao W, Luo G, Wang C-Y (2015) Modeling internal shorting process in large-format Li-ion cells. *J Electrochem Soc* 162(7):A1352–A1364
25. Zhao W, Luo G, Wang C-Y (2015) Modeling nail penetration process in large-format Li-ion cells. *J Electrochem Soc* 162(1):A207–A217
26. Yang XG, Zhang G, Wang CY (2016) Computational design and refinement of self-heating lithium ion batteries. *J Power Sources* 328:203–211
27. Zhang G, Shaffer CE, Wang C-Y, Rahn CD (2013) In-situ measurement of current distribution in a Li-ion cell. *J Electrochem Soc* 160(4):A610–A615
28. Zhang G, Shaffer CE, Wang CY, Rahn CD (2013) Effects of non-uniform current distribution on energy density of Li-ion cells. *J Electrochem Soc* 160(11):A2299–A2305
29. Zhang G, Cao L, Ge S, Wang C-Y, Shaffer CE, Rahn CD (2014) *In situ* measurement of radial temperature distributions in cylindrical Li-ion cells. *J Electrochem Soc* 161(10):A1499–A1507
30. Zhang G, Cao L, Ge S, Wang C-Y, Shaffer CE, Rahn CD (2015) Reaction temperature sensing (RTS)-based control for Li-ion battery safety. *Sci Rep* 5:18237
31. Osswald PJ, Erhard SV, Wilhelm J, Hoster HE, Jossen A (2015) Simulation and measurement of local potentials of modified commercial cylindrical cells: I: cell preparation and measurements. *J Electrochem Soc* 162(10):A2099–A2105
32. Erhard SV, Osswald PJ, Wilhelm J, Rheinfeld A, Kosch S, Jossen A (2015) Simulation and measurement of local potentials of modified commercial cylindrical cells: II: multi-dimensional modeling and validation. *J Electrochem Soc* 162(14):A2707–A2719
33. Erhard SV, Osswald PJ, Keil P, Höffer E, Haug M, Noel A, Wilhelm J, Rieger B, Schmidt K, Kosch S, Kindermann FM, Spingler F, Kloust H, Thoennessen T, Rheinfeld A, Jossen A (2017) Simulation and measurement of the current density distribution in lithium-ion batteries by a multi-tab cell approach. *J Electrochem Soc* 164(1):A6324–A6333
34. Mohammadi M, Silletta EV, Ilott AJ, Jerschow A (2019) Diagnosing current distributions in batteries with magnetic resonance imaging. *J Magn Reson* 309:106601
35. Lai X, Jin C, Yi W, Han X, Feng X, Zheng Y, Ouyang M (2021) Mechanism, modeling, detection, and prevention of the internal short circuit in lithium-ion batteries: Recent advances and perspectives. *Energy Storage Mater* 35:470–499

36. Schindler M, Durdel A, Sturm J, Jocher P, Jossen A (2020) On the impact of internal cross-linking and connection properties on the current distribution in lithium-ion battery modules. *J Electrochem Soc* 167(12):120542
37. Cavalheiro, G. M.; Iriyama, T.; Nelson, G. J.; Huang, S.; Zhang, G. (2020) Effects of nonuniform temperature distribution on degradation of lithium-ion batteries. *J Electrochem Energy Convers Storage* 17(2):021101
38. Hu Y, Iwata GZ, Mohammadi M, Silletta EV, Wickenbrock A, Blanchard JW, Budker D, Jerschow A (2020) Sensitive magnetometry reveals inhomogeneities in charge storage and weak transient internal currents in Li-ion cells. *Proc Natl Acad Sci* 117(20):10667–10672
39. Ng S-H, La Mantia F, Novak P (2009) A multiple working electrode for electrochemical cells: a tool for current density distribution studies. *Angew Chem Int Ed* 48:528–532
40. Kindermann FM, Osswald PJ, Klink S, Ehlert G, Schuster J, Noel A, Erhard SV, Schuhmann W, Jossen A (2017) Measurements of lithium-ion concentration equilibration processes inside graphite electrodes. *J Power Sources* 342:638–643
41. Finegan DP, Quinn A, Wragg DS, Colclasure AM, Lu X, Tan C, Heenan TMM, Jervis R, Brett DJL, Das S, Gao T, Cogswell DA, Bazant MZ, Di Michiel M, Checchia S, Shearing PR, Smith K (2020) Spatial dynamics of lithiation and lithium plating during high-rate operation of graphite electrodes. *Energy Environ Sci* 13(8):2570–2584
42. Teuffl T, Pritzl D, Solchenbach S, Gasteiger HA, Mendez MA (2019) Editors' choice—state of charge dependent resistance build-up in Li- and Mn-rich layered oxides during lithium extraction and insertion. *J Electrochem Soc* 166(6):A1275–A1284
43. Ohzuku T, Iwakoshi Y, Sawai K (1993) Formation of lithium-graphite intercalation compounds in nonaqueous electrolytes and their application as a negative electrode for a lithium ion (shuttlecock) cell. *J Electrochem Soc* 140(9):2490–2498
44. Yamada A, Koizumi H, Nishimura SI, Sonoyama N, Kanno R, Yonemura M, Nakamura T, Kobayashi Y (2006) Room-temperature miscibility gap in Li_xFePO_4 . *Nat Mater* 5(5):357–360
45. Bard AJ, Faulkner LR (2001) *Electrochemical methods: fundamentals and applications*, 2nd edn. Wiley, New York
46. Zhang Y, Wang C-Y (2009) Cycle-life characterization of automotive lithium-ion batteries with LiNiO_2 cathode. *J Electrochem Soc* 156:A527–A535
47. Liao, L.; Zuo, P.; Ma, Y.; Chen, X.; An, Y.; Gao, Y.; Yin, G., Effects of temperature on charge/discharge behaviors of LiFePO_4 cathode for Li-ion batteries. *Electrochim Acta* 2012, 60:269–273
48. Valoen LO, Reimers JN (2005) Transport properties of LiPF_6 -based Li-ion battery electrolytes. *J Electrochem Soc* 152(5):A882–A891
49. Laughton MA, Warne DF (2003) *Electrical engineer's reference book*, 16th edn. Elsevier, Oxford
50. Liu J, Kunz M, Chen K, Tamura N, Richardson TJ (2010) Visualization of charge distribution in a lithium battery electrode. *J Phys Chem Lett* 1:2120–2123
51. Chen Y-S, Chang K-H, Hu C-C, Cheng T-T (2010) Performance comparisons and resistance modeling for multi-segment electrode designs of power-oriented lithium-ion batteries. *Electrochim Acta* 55:6433–6439
52. Vetter J, Novák P, Wagner MR, Veit C, Möller KC, Besenhard JO, Winter M, Wohlfahrt-Mehrens M, Vogler C, Hammouche A (2005) Ageing mechanisms in lithium-ion batteries. *J Power Sources* 147(1–2):269–281
53. Omar N, Monem MA, Firouz Y, Salminen J, Smekens J, Hegazy O, Gaulous H, Mulder G, Van den Bossche P, Coosemans T, Van Mierlo J (2014) Lithium iron phosphate based battery – assessment of the aging parameters and development of cycle life model. *Appl Energy* 113:1575–1585
54. Ilott AJ, Mohammadi M, Schauerma CM, Ganter MJ, Jerschow A (2018) Rechargeable lithium-ion cell state of charge and defect detection by in-situ inside-out magnetic resonance imaging. *Nat Commun* 9(1):1776

55. Yang X-G, Ge S, Liu T, Leng Y, Wang C-Y (2018) A look into the voltage plateau signal for detection and quantification of lithium plating in lithium-ion cells. *J Power Sources* 395:251–261
56. Huang S, Du X, Richter M, Ford J, Cavalheiro GM, Du Z, White RT, Zhang G (2020) Understanding Li-ion cell internal short circuit and thermal runaway through small, slow and *in situ* sensing nail penetration. *J Electrochem Soc* 167(9):090526
57. Galvez-Aranda DE, Verma A, Hankins K, Seminario JM, Mukherjee PP, Balbuena PB (2019) Chemical and mechanical degradation and mitigation strategies for Si anodes. *J Power Sources* 419:208–218
58. Jung R, Morasch R, Karayaylali P, Phillips K, Maglia F, Stinner C, Shao-Horn Y, Gasteiger HA (2018) Effect of ambient storage on the degradation of Ni-rich positive electrode materials (NMC811) for Li-ion batteries. *J Electrochem Soc* 165(2):A132–A141
59. Li Z, Zhang J, Wu B, Huang J, Nie Z, Sun Y, An F, Wu N (2013) Examining temporal and spatial variations of internal temperature in large-format laminated battery with embedded thermocouples. *J Power Sources* 241(0):536–553
60. Huang S, Wu X, Cavalheiro GM, Du X, Liu B, Du Z, Zhang G (2019) *In situ* measurement of lithium-ion cell internal temperatures during extreme fast charging. *J Electrochem Soc* 166(14):A3254–A3259
61. Huang S, Du Z, Zhou Q, Snyder K, Liu S, Zhang G (2021) *In situ* measurement of temperature distributions in a Li-ion cell during internal short circuit and thermal runaway. *J Electrochem Soc* 168(9):090510
62. Zhou H, An K, Allu S, Pannala S, Li J, Bilheux HZ, Martha SK, Nanda J (2016) Probing multiscale transport and inhomogeneity in a lithium-ion pouch cell using *in situ* neutron methods. *ACS Energy Lett* 1(5):981–986
63. Finegan DP, Scheel M, Robinson JB, Tjaden B, Di Michiel M, Hinds G, Brett DJL, Shearing PR (2016) Investigating lithium-ion battery materials during overcharge-induced thermal runaway: an operando and multi-scale X-ray CT study. *Phys Chem Chem Phys* 18(45):30912–30919
64. Yokoshima T, Mukoyama D, Maeda F, Osaka T, Takazawa K, Egusa S (2019) Operando analysis of thermal runaway in lithium ion battery during nail-penetration test using an X-ray inspection system. *J Electrochem Soc* 166(6):A1243–A1250